Periodic hyperdamping inclusions in resonant metamaterials for control of broadband vibroacoustic energy

Undergraduate Honors Thesis

Presented in Partial Fulfillment of the Requirements for Graduation with Distinction
in the Department of Mechanical and Aerospace Engineering of The Ohio State University

By

Justin Bishop

April 2017

Thesis Committee:

Ryan L. Harne, Advisor

Kiran D'Souza

ABSTRACT

The absorption of structural vibrations and noise is often essential to structural integrity and operator safety. These unwanted vibroacoustic energies are typically broadband, which presents a challenge to traditional resonance-based dampers. Additionally, low frequency vibrations and noise are particularly difficult to absorb in situations where lightweight solutions are required. Recent studies have shown that utilizing the elastic stability limit, or buckling point, can lead to a theoretically unbounded increase in damping ratio. Additionally, by embedding distributed masses within acoustic foams, damping is increased far beyond the capabilities of foam alone. By taking advantage of both this near-buckling phenomenon and distributed masses, this research investigates periodically arranged hyperdamping inclusions within foam for lightweight, broadband vibroacoustic damping capabilities. Behavior of hyperdamping metamaterial arrays is numerically and experimentally characterized. Acoustic models suggest that hyperdamping inclusions are more effective at noise absorption when spread apart, which is reflected in an acoustic and a vibration experimental study. An investigation of various arrangements of inclusions shows that having multiple inclusions perpendicular to the wave propagation axis is more effective than having multiple inclusions along the direction of wave propagation, which suggests that a plane of distributed inclusions most effectively increases vibroacoustic energy absorption. Hyperdamping inclusion arrays are demonstrated to be robust, in that hyperdamping architectures which are intentionally “mistuned” away from the elastic stability limit are still highly effective for broadband attenuation of waves. Hyperdamping inclusions are compared to traditional solid elastomer inclusions, and are shown to have comparable or increased energy absorption while weighing less. These findings demonstrate a new idea for a lightweight, broadband damping material system. The broad applications of this system include numerous vehicle systems, where weight is key to performance and high levels of energy dissipation are required.

ACKNOWLEDGEMENTS

I first and foremost thank my advisor Dr. Ryan Harne for his support, encouragement, and unbounded expertise.

I also want to thank Dr. Kiran D'Souza for his support and help as a committee member.

Thanks to the College of Engineering for their support in the form of an undergraduate research scholarship.

All related experiments in this research are conducted in the Laboratory of Sound and Vibration Research (LSVR), directed by Dr. Ryan Harne.

TABLE OF CONTENTS

LIST OF FIGURES

LIST OF TABLES

1 INTRODUCTION

1.1 Vibroacoustic energy and damping

Vibroacoustic energy, which is a combination of vibration energy and acoustic energy, comes from many sources, including internal sources such as engines, thrusters, and turbines, and external sources such as road to wheel vibration and fluid turbulence. Absorption of structural vibrations and noise are essential to the function of operators, machinery, and equipment. Energy can come from harmonic excitations such as engines, but typically comes from spectrally broadband sources. Low frequency vibrations have proven particularly difficult to dissipate due to the larger amplitudes at these frequencies [1] and ineffectiveness of traditional acoustic foams in this frequency band [2]. Vibroacoustic energy absorption or attenuation methods have been explored by many researchers in diverse fields over the years, due to the need for material systems with ever increasing performance [3].

1.2 Significance of research

Unwanted vibroacoustic energies still present a problem for a wide range of applications and engineered systems. Traditional damping methods introduce significant mass to the system, and in many applications, such as automotive and aerospace, lightweight solutions are critical to efficiency [4]. While acoustic foams can effectively attenuate waves in the mid- to high-frequency range, they are less effective at low frequency damping [2]. Damping panels are often used in combination with acoustic foams to enhance low frequency damping, yet these panels add significant mass which is not always practical. Broadband, lightweight vibroacoustic attenuators are in high demand, due the need for high performance engineered systems [5].

1.3 Recent developments in broadband damping

Resonant metamaterials show promising bandgap energy attenuation, which absorbs large amounts of energy in tunable bands [1]. These resonant metamaterials achieve high stiffness and high damping through the use of internally resonating lattices within an external frame. Yet, these bands are often narrowband and parameter sensitive, which makes them ineffective for situations requiring a robust, broadband energy attenuating material system. Most proposed resonant metamaterials are also made of dense materials including metals and heavy rubbers [6], which are impractical in situations where lightweight solutions are critical. On the other hand, large and broadband attenuation capabilities have been achieved by periodic elastic metamaterials that leverage instability mechanisms and negative stiffness [7] [8] [9]. These materials utilize a cancellation of positive and negative stiffness to achieve extreme damping. Yet, these too are often materials such as acrylic [8], epoxy [9], 3D-printed polymers [10] and other dense materials which may add significant mass relative to traditional vibroacoustic attenuators [7].

Researchers have additionally begun to utilize buckling instability to achieve broadband energy attenuation [11] [12]. Shan et al have achieved remarkable energy capture and impact resilience through the use of multiple folding mechanisms, which utilizes a parameter sensitive geometry to induce buckling phenomena [13]. These buckling phenomena typically require active stress or compression to achieve the correct tuning, while a passive system is needed for many applications [11] [14]. Additionally, current mechanisms which

utilize buckling phenomena are typically dense, and add significant mass to the engineered system which they are protecting.

While buckling phenomena are known to enhance energy attenuation [15], utilizing the point of buckling rather than utilizing post-buckled phenomena should theoretically provide higher attenuation, due to the cancellation of the positive and negative stiffnesses. This cancelation, termed the *elastic stability limit* [16], eliminates the fundamental natural frequency $\omega_n \rightarrow 0$. In fact, the damping ratio at the elastic stability limit grows theoretically without bound [17] due to the relation for damping ratio $\zeta = c / 2m\omega_n$ where c and m are the damping constant and mass, respectively [18]. Despite recent advances, the use of dense materials and reliance on parameter-sensitive resonance phenomena make these implementations insufficient for lightweight, broadband energy absorption applications. Hyperdamping metamaterials are the first realization of a lightweight, robust implementation of critical point damping, for capturing impact energy [19], vibration, and acoustic energy [20]. By utilizing the elastic stability limit, hyperdamping materials can be used in many situations and configurations, including within foams, box beams, and sandwich panels.

One promising way to enhance the low frequency energy attenuation capabilities of foam, is the use of periodically arranged inclusions within poroelastic foam. These metamaterials of inclusions within foam have been shown to significantly improve broadband damping [21] [22], due to the inclusions behaving as distributed mass-spring-dampers [23]. These inclusions, which are typically solid metals have been shown to improve low frequency vibration and noise attenuation, at a cost of increasing the system mass [24]. These distributed inclusions in foam, known commonly as heterogeneous (HG) blankets, are a metamaterial which can greatly increase transmission loss for noise and vibration control [25]. Utilizing resonance phenomena can significantly reduce the mass of the HG blankets [26], yet results in narrowband absorption which is not always sufficient when truly broadband energy capture is required [27]. The effectiveness of variety of inclusion shapes beyond small spheres has been examined theoretically and experimentally by Groby et al. who found that the filling fraction of inclusions within the foam was found to affect the absorption more than the shape of the inclusion [28].By combining the concepts of hyperdamping inclusions and periodically arranged inclusions, this research seeks to develop a passive, lightweight, broadband energy capture material system.

1.4 Research goal

The goal of this research is to numerically and experimentally characterize the behavior of hyperdamping metamaterials, which are composed of periodically arranged hyperdamping inclusions within foam, for noise and vibration attenuation capabilities. To achieve this goal, finite element models are created to determine the acoustic absorption coefficient of the metamaterials and the influence of varied inclusion spacing and arrangement. Then through acoustic experiments, models are verified and refined. Additional vibration experiments are conducted to subject metamaterial specimens to higher energy inputs and examine force transmissibility. These experiments and models allow for comparisons in order to determine energy capture enhancements achieved by the hyperdamping metamaterials when compared to the foam media itself and to resonant metamaterials.

1.5 Overview of thesis

This thesis is organized as follows. Chapter 2 discusses hyperdamping metamaterial design and finite element modeling of hyperdamping metamaterials. Chapter 3 describes the data acquisition apparatus and test methods used in the experiments, including both acoustic testing and vibration testing. Chapter 4 presents the experimental results, and provides numerous discussions on the experimental trends that provide new insights regarding the broadband damping capabilities of periodically arranged hyperdamping metamaterials. Chapter 5 summarizes the key experimental discoveries of this research and proposes future research directions.

2 HYPERDAMPING METAMATERIALS

2.1 Design of hyperdamping metamaterials

The realization of hyperdamping inclusions utilized in this thesis is based on architected elastomer constrained within aluminum shells. Fabrication of hyperdamping inclusions follows the steps taken by Harne et al. in a recent characterization of hyperdamping metamaterials containing one inclusion [20]. ABS molds are 3D printed (FlashForge Creator Pro) as the negative of the elastomer in two parts, as shown in Figure 1. The molds are coated with a release spray (Smooth-On, Inc., Ease Release 200) and sealed together with a small bead of wax. Silicone rubber (Smooth-On, Inc., Mold Star 15S) is poured into the molds, and cured at room temperature for the recommended time, before being removed from the mold. The aluminum shells of inner diameter 16.56 mm and thickness 1.25 mm are cut to 19 mm in length, as is the elastomer after sufficient curing time. The elastomer is then cleaned with water to remove dust and wax, carefully inserted into the shell, and gently manipulated to ensure it seats correctly.

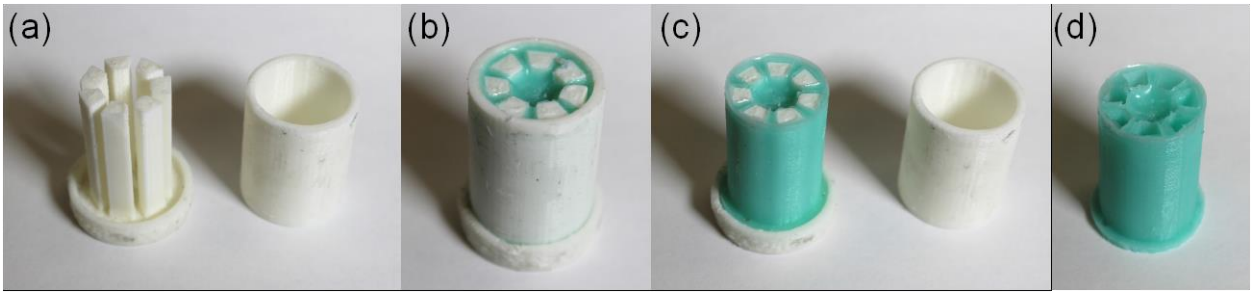

Figure 1: Molding process: (a) 3D printed mold pieces before joining and sealing with wax, (b) after pouring elastomer and allowing recommended curing time, (c) after breaking wax seal and removing shell, (d) after carefully removing from base mold. Elastomer is then cut to length and washed.

A number of parameters can be adjusted to ensure the inclusion is very near to the elastic stability limit, or buckling point. In this thesis, rotationally symmetric inclusion designs are utilized, which allow for a global buckling to occur [20]. To achieve the critical constraint of the buckling point, the ratio of open to closed angle and the ratio of inclusion outer diameter to shell inner diameter are chosen. Variation of the open angle ratio is effectively a way to adjust beam thickness, which governs the buckling point [20]. Change of the diameter ratio is effectively a way to adjust the compression of the inclusion to induce buckling. A parametric finite element (FE) study is conducted in COMSOL Multiphysics, where both open angle ratio and diameter ratio are adjusted over the range of values which can be fabricated. By plotting the fundamental eigenfrequency, the buckling horizon is determined as the line along which the eigenfrequency becomes purely imaginary [20]. This is seen in Figure 2, where any dark blue region is post-buckled.

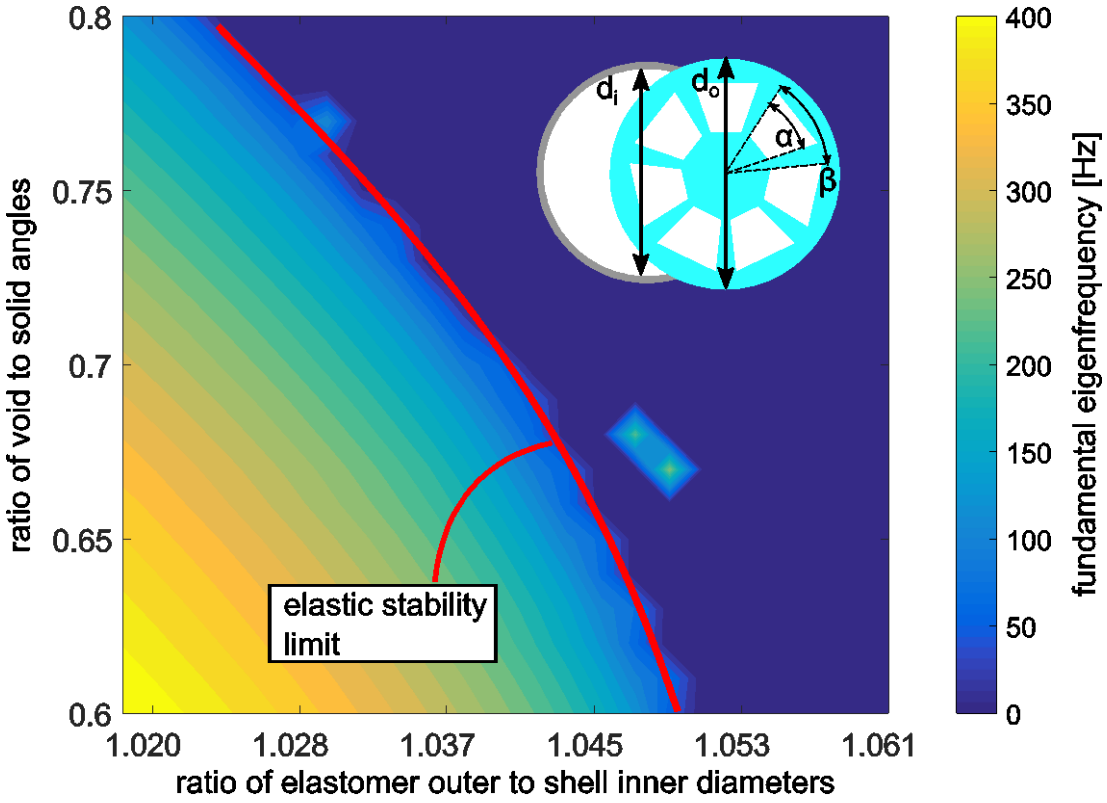

Figure 2: Fundamental eigenfrequency plot showing elastic stability limit and the parameters varied to achieve it. The rectangle outside the elastic stability limit "horizon" is likely a numerical error corresponding to two distinct configurations.

Three architectures are molded, using a constant open angle ratio of 0.67. The architectures otherwise are designed with diameter ratios of 1.0325, 1.0455, and 1.0547, where the first is not yet buckled, the second is very near to buckling, and the third is post-buckled, as guided by the FE model. This can be seen in Figure 3,where a control solid elastomer inclusion is shown beside three hyperdamping inclusions showing no rotation, very slight rotation, and clear rotation, respectively. Thus, only the diameter ratio influences the nearness to buckling.

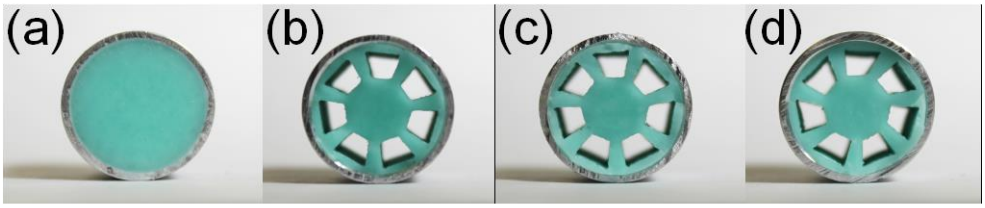

Figure 3: Four inclusion architectures used: (a) control solid elastomer inclusion and three hyperdamping inclusion s, which are (b) not buckled, (c) very nearly buckled, and (d) post-buckled.

Foam samples (The Foam Factory Super Soft Foam) are cut to size, and then cut in half at locations where inclusions will be inserted. From each half, a triangular wedge of foam is removed. The portions of the remaining channel where in an inclusion will be placed are left empty, while the wedge is cut down to size

and reinserted around these locations. This process can be seen in Figure 4, which illustrates the fabrication steps for one half of a final test specimen. Adhesive (HDX Spray Adhesive and 3M Super 77 Spray Adhesive) is used on all cut surface to ensure the foam and inclusion are held together, as seen in Figure 5. For test specimens with multiple inclusions, multiple channels are cut or multiple inclusions are placed into each channel, depending on the configuration of the specimen.

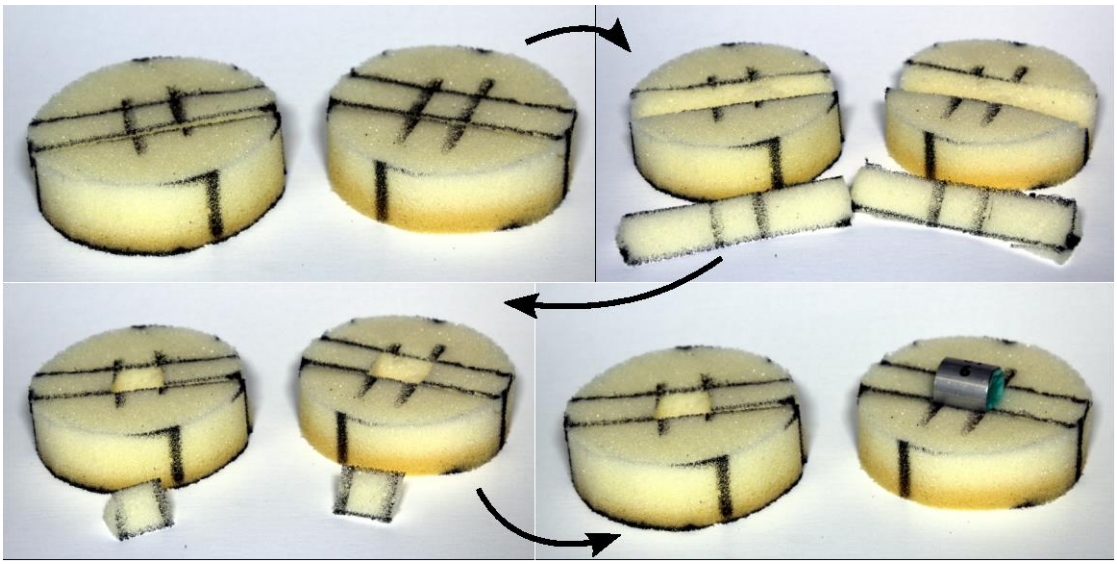

Figure 4: Fabrication steps of hyperdamping metamaterials: Cutting foam in half, removing channel, replacing foam, adding inclusion.

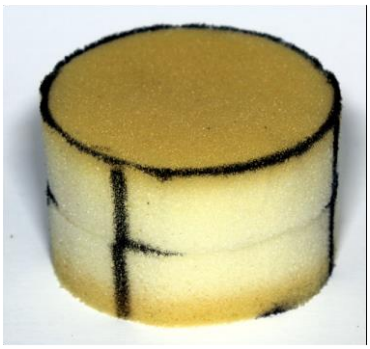

Figure 5: Foam sample after spray gluing, with the line of glue visible around the edge. Two of these 50 mm samples are glued together to create a full 100 mm test specimen.

2.2 Modeling hyperdamping metamaterials

To gain insight into the acoustic behavior of periodic hyperdamping inclusions in foam, a finite element model is created in COMSOL Multiphysics. To accurately model the metamaterial, a multi-domain model is needed with air, foam, shells, and inclusions, as seen in Figure 6. A phenomenological model is used rather than a model which recreates the buckling phenomena of the inclusions, due to the already complex nature of the model. This phenomenological model uses an artificially high damping within the solid domain of the inclusion, as seen in Figure 6, such that the inclusions behave similarly to inclusions which

are near to the elastic stability limit. Because of the geometry of the inclusion arrays, a 3D model is necessary, which significantly increases the computational cost of the model.

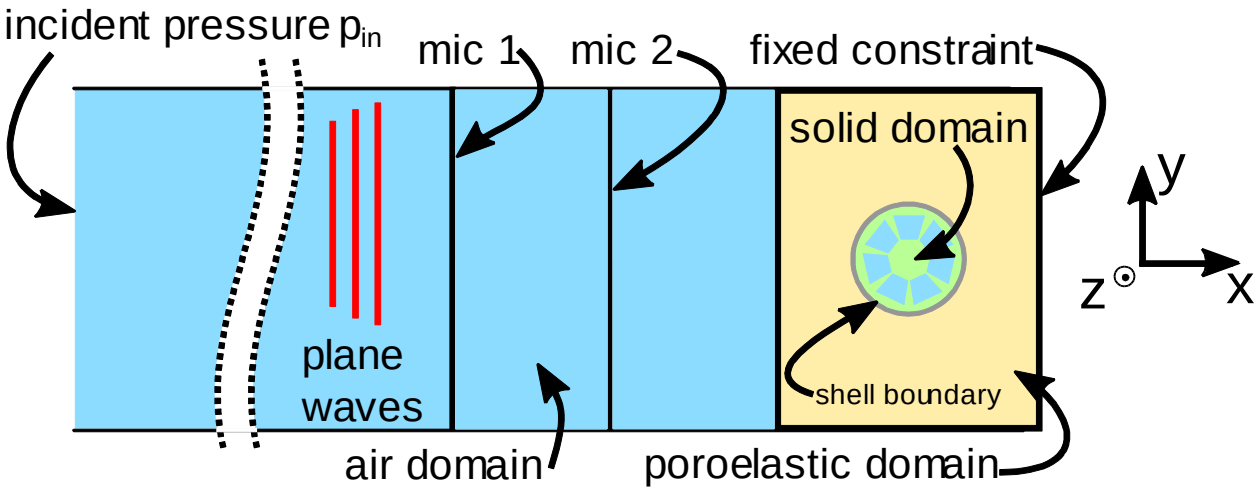

Figure 6: Acoustic model setup showing key boundary conditions and domain types

The model is set up with a unit pressure input p_{in} along the left face, with a fixed constraint along the right face of the foam. All cylindrical edges are constrained to move only along the direction of wave propagation, to recreate the boundary conditions of a standing wave tube. The air is considered as an acoustic domain and the foam is a poroelastic domain. Additional air is located in the voids of each inclusion. Any boundary between foam and air is treated as an acoustic-porous boundary. The boundary between the solid domain inclusion and the foam is treated as a shell boundary. The boundary between inclusion and voids is a solid-acoustic boundary, and between the inclusion and foam on top and bottom is a solid-porous boundary. If any boundary is not correctly created, the absorption of the specimen will be nearly 100 % across all frequencies, because the model cannot resolve the behavior of the model at undeclared boundaries.

To reduce computational cost, a coarse mesh is used on the air and foam. This mesh size s_{max} is limited by

$$s_{max} = \frac{c}{10 f_{hi}} \tag{1}$$

where c is the speed of sound, and f_{hi} is the highest frequency of interest. A frequency sweep is performed from 10 Hz to 2010 Hz, which is close to the range of the standing wave tube. Average pressure is measured at the locations of mic 1 and 2, which are set to be the same locations as the locations of the standing wave tube. Absorption coefficient can then be found by taking transfer functions between the microphones. The measured transfer function is defined by

$$\tilde{H}(f) = \frac{G_{xy}(f)}{G_{xx}(f)} = \frac{X(f)Y^*(f)}{X(f)X^*(f)} \tag{2}$$

where G_{xy} is the cross power spectrum between microphone 1 and 2, G_{xx} is the auto power spectra of microphone 1, X(f) is the FFT of the microphone 1 pressure x(t), Y(f) is the FFT of the microphone 2 pressure y(t), and * denotes the complex conjugate [29]. Complex reflection coefficient is calculated as

$$\widetilde{\boldsymbol{R}} = \frac{\widetilde{\boldsymbol{H}} - \boldsymbol{e}^{\boldsymbol{jkS}}}{\boldsymbol{e}^{-\boldsymbol{jkS}} - \widetilde{\boldsymbol{H}}} \boldsymbol{e}^{-\boldsymbol{j2k}(\boldsymbol{l}+\boldsymbol{S})} \quad 3$$

where *S* is the microphone spacing in meters, *l* is the distance from the specimen to the nearest microphone in meters, and *k* is the wavenumber defined as

$$\boldsymbol{k} = \frac{\boldsymbol{2\pi f}}{\boldsymbol{c_0}} \quad 4$$

where c_0 is the speed of sound, 343 m/s. From reflection coefficient, absorption coefficient is then calculated as

$$\boldsymbol{\alpha} = \mathbf{1} - \left|\widetilde{\boldsymbol{R}}\right|^{\mathbf{2}} \quad 5$$

Poroelastic models are governed by seven parameters, of which only Young's modulus, Poisson's ratio, density, and porosity can be easily measured or are known from the manufacturer. Young's modulus is calculated by measuring displacement and load in a load frame with a specimen of known thickness and cross-sectional area. Then

$$E = \frac{k\Delta L}{A}$$

where k is the stiffness measured by dividing load by displacement, ΔL is the deformed length, and A is the cross sectional area. Poisson's ratio and porosity are assumed to be 0.44 and 0.99, which are within the range of similar foams [30]. Density is listed by the manufacturer [31]. The other three parameters are Biot-Willis coefficient, tortuosity, and permeability. To accurately model the foam, absorption coefficient is measured in a standing wave tube, and then imported into the finite element modeling software. Curve fitting is performed with the three unknown parameters, in order to best match the experimental data to the model.

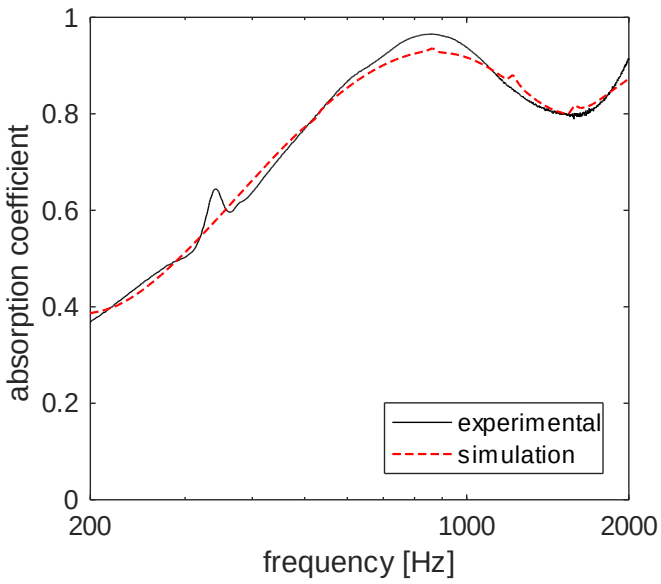

Figure 7: Absorption coefficient comparison between experiment and simulation for a 100 mm foam sample

From Figure 7, it is seen that the model and experiment agree very well in the range of 200 Hz to 2000 Hz. Below this range, the model diverges from experiment because the model converges on 0, while the experiment converges near 0.2. The seven foam properties which results in this curve fit are summarized in Table 1.

Table 1: Foam material properties used for simulations to match simulation to experimental data

Young's modulus [kPa]	Poisson's ratio	Density [kg/m^3]	Porosity	Biot-Willis coefficient	Tortuosity	Permeability [m^2]
20.301	0.44	19.222	0.99	0.87	1.29	4.5e-09

A study is conducted for two hyperdamping inclusions with varied spacing, to gain insight into the interactions of two hyperdamping inclusions. Inclusion material properties are taken from prior literature [20] to be ν=0.33 and E=200×10^9. Shells are modeled with standard 6061 aluminum material properties. Two inclusions are initially placed side-by-side within a 100 mm long by 85 mm diameter sample of foam and then brought farther apart along the direction of wave propagation, as illustrated in Figure 8. Inclusions are aligned in the z direction, and spaced 38 mm apart in the y direction. The spacing in the direction of wave propagation, the x axis, is varied from 0 cm where the inclusions are aligned, to 6 cm where the inclusions are very near to the edge of the foam sample.

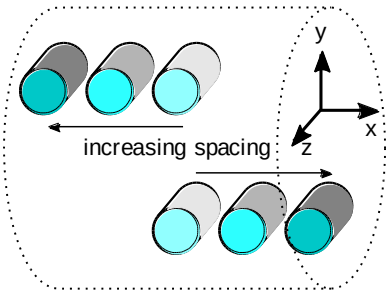

Figure 8: Schematic showing arrangement of inclusions with varying spacing along the axis of wave propagation

The results of the study can be seen in Figure 9. From this, it can be seen that the addition of two inclusions is expected to increase the absorption coefficient in the range of 300 Hz to 1000 Hz. Below this range, the model becomes inaccurate due to the model absorption coefficient converging to 0, which is not reflected in experiment. While the model does not show much distinction between the spacings in the range of 300 Hz to 1000 Hz, it does show significant distinction above this range. Above 1000 Hz, the inclusions which are side by side actually have a lower absorption coefficient than the foam only, while the inclusions which are spaced at 6 cm have a higher absorption coefficient. This suggests that increasing the spacing between hyperdamping inclusions will increase their effectiveness at high frequencies, without influencing their performance at lower frequencies.

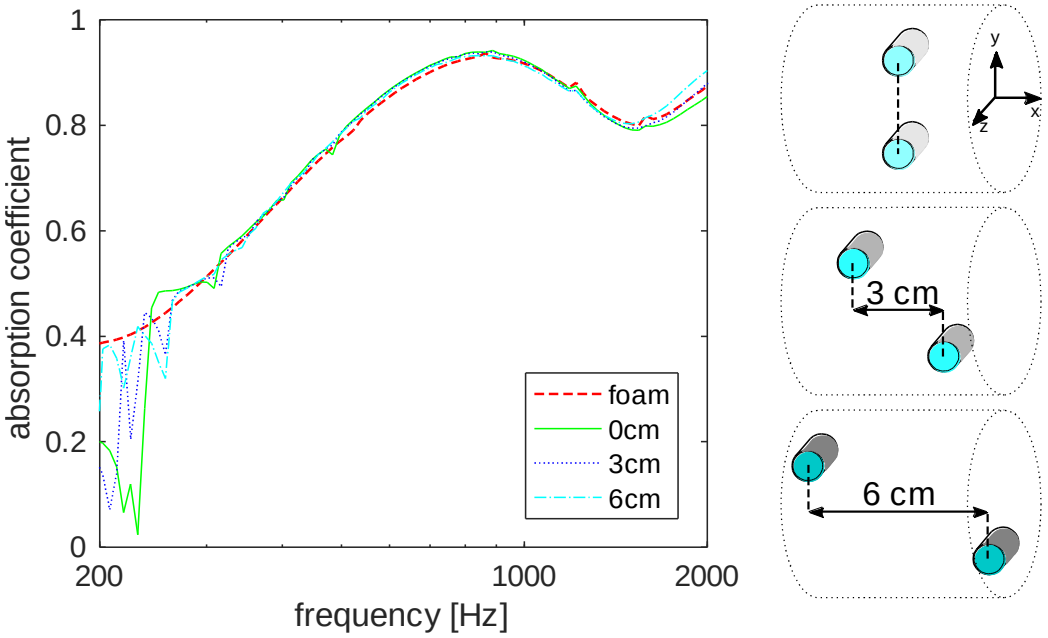

Figure 9: Finite element absorption coefficient for two hyperdamping inclusions of varied spacing, compared to a foam only simulation

Next, three distinct arrangements of two inclusions are considered. The arrangements are aligned with the axis of wave propagation as the x axis, and the axis of the cylindrical inclusions as the z axis. Based on the observation that hyperdamping inclusions are more effective when spread out, the spacing between two inclusions in the axis of wave propagation is 50 mm center-to-center, and for two inclusions in the y or z

direction, it is 38 mm center-to-center. This is limited by the diameter of the standing wave tube, such that the inclusions are not close to the edge of the tube. From Figure 10, it is shown that the model has little distinction between the three arrangements. In fact, the 1x2x1 and 1x1x2 arrangements have nearly identical absorption coefficient. This suggests that the model does not predict that the two inclusions will have meaningful interaction, because the inclusions should vibrate in the x and y directions but not in the z direction. Thus, if the model shows a distinction between the 1x2x1 and 1x1x2 arrangements then it shows that the inclusions do have interactions. The 2x1x1 arrangement is distinct from the other two arrangements, and is slightly less effective in the range of 400 Hz to 1000 Hz, but slightly more effective above this range.

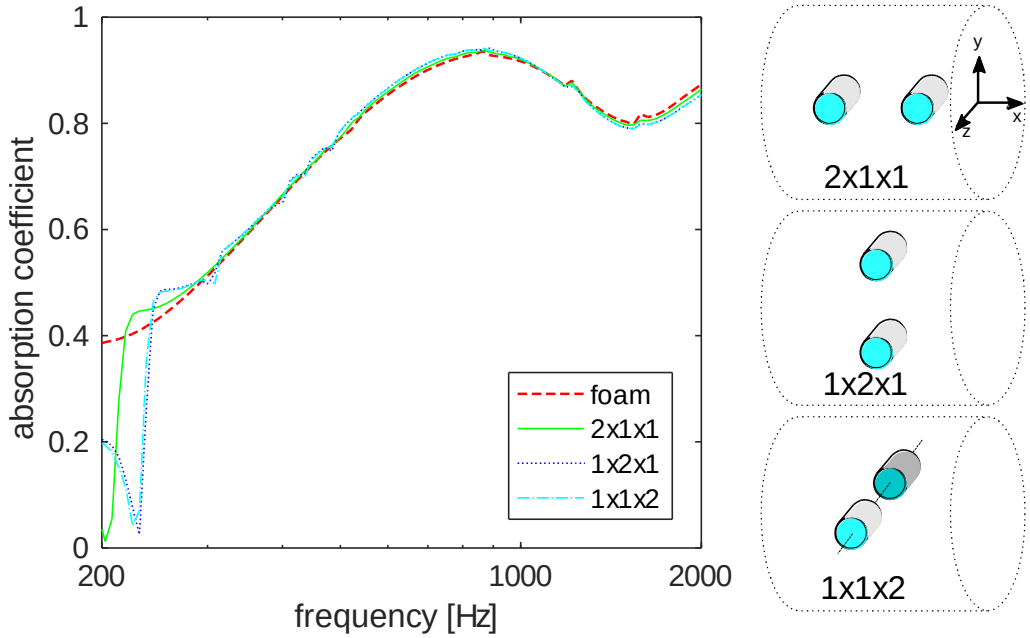

Figure 10: Finite element absorption coefficient for three arrangements of two hyperdamping inclusions, compared to a foam only simulation

3 EXPERIMENTAL METHODS

3.1 Acoustic testing sensors, equipment, and data acquisition methods

Guided by the simulation results, a standing wave tube, or impedance tube, is used to measured absorption coefficient using a standard 2-microphone method [29]. A sound source at one end of the tube is located sufficiently far from the microphones such that plane waves develop before reaching the microphones, as seen in Figure 11. A rigid termination is located after the specimen. A transfer function between the two microphones (PCB 130E20) is taken to determine absorption coefficient, which is a measure of how much of the incoming waves are attenuated within the specimen [29].

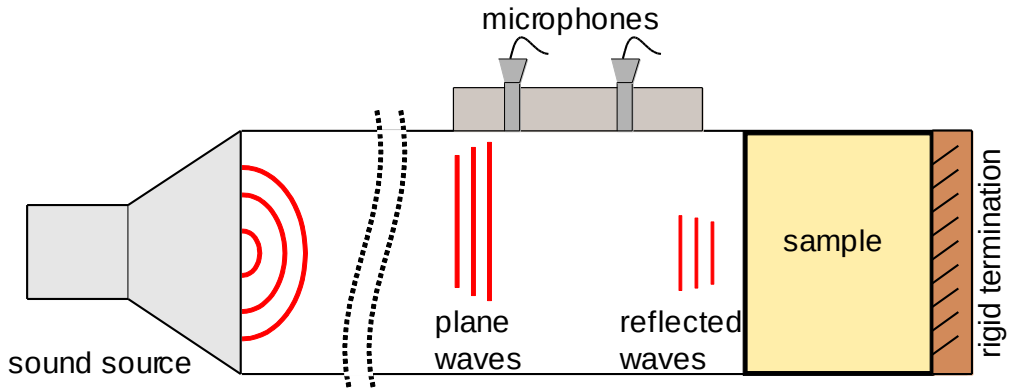

Figure 11: Impedance tube schematic

White noise is generated by a computer, which is connected to an amplifier input (AudioSource AMP 100) and DAQ system (NI USB-6341). The amplifier output is connected directly to the sound source. Two microphones (PCB 130E20) are connected to a signal conditioner (PCB 482C05), which is connected to the DAQ system analog inputs. Data is sampled at 65536 Hz for 40 seconds, and bandpass filtered from 40 Hz to 3000 Hz. The lower bound of testable frequency range is

$$f_{min} = \frac{0.01c_0}{S} = \frac{3.43}{S} \tag{6}$$

which for this tube is 45 Hz and the upper bound is

$$f_{max} = \min\begin{cases} \frac{0.586c_0}{d} = \frac{201}{d} \\ \frac{0.8c_0}{2S} = \frac{1372}{S} \end{cases} \tag{7}$$

which for this tube is limited by the tube diameter of 76.2 mm, resulting in an upper limit of 2638 Hz. The data is averaged over a 40 second data acquisition period. To compute absorption coefficient, the impedance tube must first be calibrated by inserting any specimen and testing with both the standard configuration, and a switch configuration in which the microphone locations are physically switched. The calibration factor is then

$$\widetilde{\boldsymbol{H}}_{\boldsymbol{c}} = \left(\widetilde{\boldsymbol{H}}^{\boldsymbol{I}}\widetilde{\boldsymbol{H}}^{\boldsymbol{II}}\right)^{\frac{\mathbf{1}}{\mathbf{2}}} = \left|\widetilde{\boldsymbol{H}}_{\boldsymbol{c}}\right|\boldsymbol{e}^{\boldsymbol{j}\boldsymbol{\phi}_{\boldsymbol{c}}} \quad 8$$

where H^I is the previously defined transfer function for the standard configuration, and H^{II} is the transfer function for the switched configuration. Then,

$$\boldsymbol{H} = \frac{\widetilde{\boldsymbol{H}}}{\widetilde{\boldsymbol{H}}_{\boldsymbol{c}}} \quad 9$$

where $\widetilde{H}$ is the measured transfer function. Reflection coefficient is then

$$\widetilde{\boldsymbol{R}} = \frac{\widetilde{\boldsymbol{H}} - \boldsymbol{e}^{\boldsymbol{jkS}}}{\boldsymbol{e}^{-\boldsymbol{jkS}} - \widetilde{\boldsymbol{H}}}\boldsymbol{e}^{-\boldsymbol{j2k}(\boldsymbol{l}+\boldsymbol{S})} \quad 10$$

and absorption coefficient is

$$\boldsymbol{\alpha} = \mathbf{1} - \left|\widetilde{\boldsymbol{R}}\right|^{\mathbf{2}} \quad 11$$

Octave band and one-third octave band, which are standard industry measures, are then computed by

$$\boldsymbol{\alpha}_{\boldsymbol{OB}} = \frac{\mathbf{1}}{\boldsymbol{n}}\sum_{\boldsymbol{i}=\mathbf{1}}^{\boldsymbol{n}}\boldsymbol{\alpha}_{\boldsymbol{fi}} \quad 12$$

where *n* is the number of frequency bins in the octave band or one-third octave band and *fi* is a frequency bin in the desired octave or one-third octave band. The octave bands located within the frequency range of the standing wave tube are

Table 2: Octave bands contained within standing wave tube frequency range

Lower Band Limit [Hz]	Center Frequency [Hz]	Upper Band Limit [Hz]
44.2	62.5	88.4
88.4	125	176.8
176.8	250	353.6
353.6	500	707.1
707.1	1000	1414.2

and the one-third octave bands are

Table 3: one-third octave bands contained within standing wave tube frequency range

Lower Band Limit [Hz]	Center Frequency [Hz]	Upper Band Limit [Hz]
44.2	49.6	55.7
55.7	62.5	70.2
70.2	78.7	88.4
88.4	99.2	111.4
111.4	125	140.3
140.3	157.4	176.8
176.8	198.4	222.7
222.7	250	280.6
280.6	315	353.6
353.6	396.9	445.4
445.4	500	561.2
561.2	630	707.1
707.1	793.7	890.9
890.9	1000	1122.5
1122.5	1259.9	1414.2
1414.2	1587.4	1781.8

For transmission loss measurement, the rigid termination of the impedance tube is replaced by an additional length of tube, as seen in Figure 12. This additional tube has two microphones between the specimen and an anechoic termination. A two-load method is utilized to measure transmission loss, where the specimen is tested first with an open-ended tube and then with an anechoic termination [32]. The only change to the DAQ system used for the impedance tube setup is the addition of two microphones (PCB 130E20).

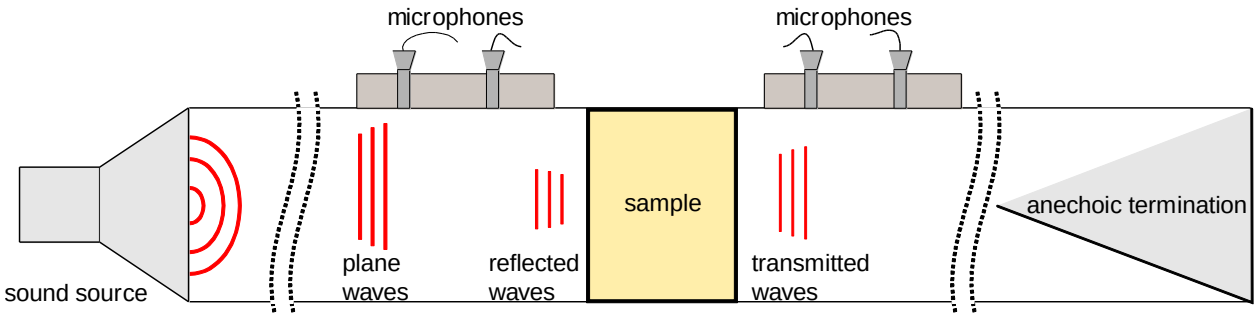

Figure 12: Transmission loss tube schematic. Anechoic termination is removed for open-ended tests

For each microphone, the measured transfer function is

$$\boldsymbol{H_{n,ref} = \frac{G_{n,ref}}{G_{ref,ref}}} \tag{13}$$

where $G_{n,ref}$ is the cross power spectrum to the reference signal and $G_{ref,ref}$ is the reference autospectrum. Complex pressure amplitude is then calculated for both upstream and downstream direction of the specimen, and for both positive and negative phase, which are defined as

$$\boldsymbol{A = j\frac{H_{1,ref}e^{-jkl_1} - H_{2,ref}e^{-jk(l_1+s_1)}}{2\sin ks_1}} \tag{14}$$

$$\boldsymbol{B = j\frac{H_{2,ref}e^{jk(l_1+s_1)} - H_{1,ref}e^{jkl_1}}{2\sin ks_1}} \tag{15}$$

$$\boldsymbol{C = j\frac{H_{3,ref}e^{jk(l_2+s_2)} - H_{4,ref}e^{jkl_2}}{2\sin ks_2}} \tag{16}$$

$$\boldsymbol{D = j\frac{H_{4,ref}e^{-jkl_2} - H_{3,ref}e^{-jk(l_2+s_2)}}{2\sin ks_2}} \tag{17}$$

where s_1 and s_2 are the spacing between the upstream microphones and downstream microphones respectively, and l_1 and l_2 are the distances from the specimen front face to the nearest microphone on the upstream and downstream side, respectively [32]. From these, the acoustic pressure and particle velocity on both faces of the specimen (x=0 and x=d) are found to be

$$\boldsymbol{p_o = A + B} \tag{18}$$

$$\boldsymbol{p_d = Ce^{-jkd} + De^{jkd}} \tag{19}$$

$$\boldsymbol{u_0 = \frac{A - B}{\rho c}} \tag{20}$$

$$\boldsymbol{u_d = \frac{Ce^{-jkd} - De^{jkd}}{\rho c}} \tag{21}$$

Then, the transfer matrix for the specimen is calculated for each load case

$$\boldsymbol{T = \begin{bmatrix} \frac{p_{0a}u_{db} - p_{0b}u_{da}}{p_{da}u_{db} - p_{db}u_{da}} & \frac{p_{0b}p_{da} - p_{0a}p_{db}}{p_{da}u_{db} - p_{db}u_{da}} \\ \frac{u_{0a}u_{db} - u_{0b}u_{da}}{p_{da}u_{db} - p_{db}u_{da}} & \frac{p_{da}u_{0b} - p_{db}u_{0a}}{p_{da}u_{db} - p_{db}u_{da}} \end{bmatrix}} \tag{22}$$

where a denotes the anechoic termination case and b denotes the open ended case. The transmission coefficient of the specimen is defined as

$$t = \frac{2e^{jkd}}{T_{11} + \left(\frac{T_{12}}{\rho c}\right) + \rho c T_{21} + T_{22}} \quad (23)$$

and the transmission loss of the specimen is

$$TL = 20 \log_{10} \left|\frac{1}{t}\right| \quad (24)$$

which, due to the use of a standing wave tube measurement, is more specifically referred to as normal transmission loss, due to the normal incidence of the sound source. Transmission loss, more generally, is a measure of the ratio of incident power W_i to transmitted power W_t defined as

$$TL = 10 \log_{10} \left|\frac{W_i}{W_t}\right| \quad (25)$$

3.2 Force transmissibility sensors, equipment, and data acquisition methods

Force transmissibility is measured by using an electrodynamic shaker (Labworks LT-140-110) to excite specimens. A force transducer between the shaker and specimen (PCB 208C02) measures the input force, and a second force transducer (PCB 208C01) between the specimen and a rigid termination measures the output force as seen in Figure 13. An accelerometer (PCB 352C33) and the two force transducers are connected to a signal conditioner (PCB 482C05). The accelerometer signal is then used by the shaker controller (Vibration Research VR 9500), which is input to the shaker amplifier (Labworks PA-141). The signal conditioner output is connected to a DAQ system analog input (NI PXIe-6368 card within NI PXIe-1073 chassis). The entire test setup is rigidly fixed to an isolation table (Newport SMART TABLE UT2). The controller is given time to ramp-up the excitation to 0.1 m/s^2 RMS (root mean square) across the frequency band of 20 Hz to 600 Hz before data is collected. Data is sampled at 8192 Hz and bandpass filtered from 20 Hz to 600 Hz. The data is averaged over a 60 second data collection period. For this low level of RMS acceleration, the linear force transmissibility is computed as the frequency domain transfer function between the output to input force.

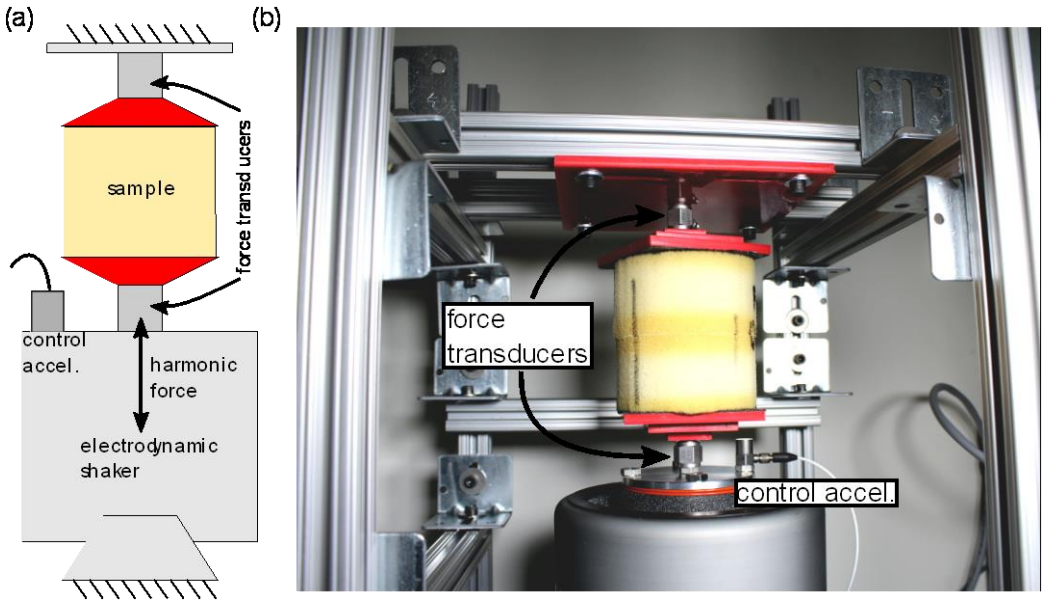

Figure 13: Force transmissibility (a) schematic and (b) test setup

4 RESULTS AND DISCUSSION

4.1 Influence of spacing between inclusions

Rigid inclusions in poroelastic media are shown to have an effective area, or footprint, over which the stiffness of the distributed mass-spring-damper can be considered [22]. To investigate the footprint of hyperdamping inclusions, two inclusions are initially placed side-by-side within a 100 mm long by 85 mm diameter sample of foam and then moved farther apart along the direction of wave propagation, in the same manner as the simulation. Inclusions are aligned in the z direction, and spaced 38 mm apart in the y direction. The spacing in the direction of wave propagation, the x axis, is varied from 0 cm where the inclusions are aligned, to 6 cm where the inclusions are very near to the edge of the foam sample.

The results of this study are presented in Figure 14. As seen in Figure 14 (a), absorption coefficient is lower for the control solid elastomer inclusions at 0 cm spacing and at 6 cm spacing, compared to the sample of foam alone. This may be due to the aluminum shell reflecting more sound waves than the foam would alone. Because the foam samples are 100 mm thick, their absorption is already quite high, which makes increasing it difficult. For the control solid elastomer inclusions at 3 cm spacing, absorption coefficient is increased in the range of 100 Hz to 1000 Hz. Figure 14 (b) shows the transmission loss for the control solid elastomer inclusions of varied spacing. From this, it can be seen that the 0 cm and 6 cm spacings decrease the transmission loss in the range of 100 Hz to 250 Hz and 400 Hz to 1000 Hz. However, in the range of 250 Hz to 400 Hz, transmission loss is significantly increased. The 3 cm spacing is again the most effective, as it increases the transmission loss across the entire frequency range, and increases transmission loss by the most in the 250 Hz to 400 Hz range.

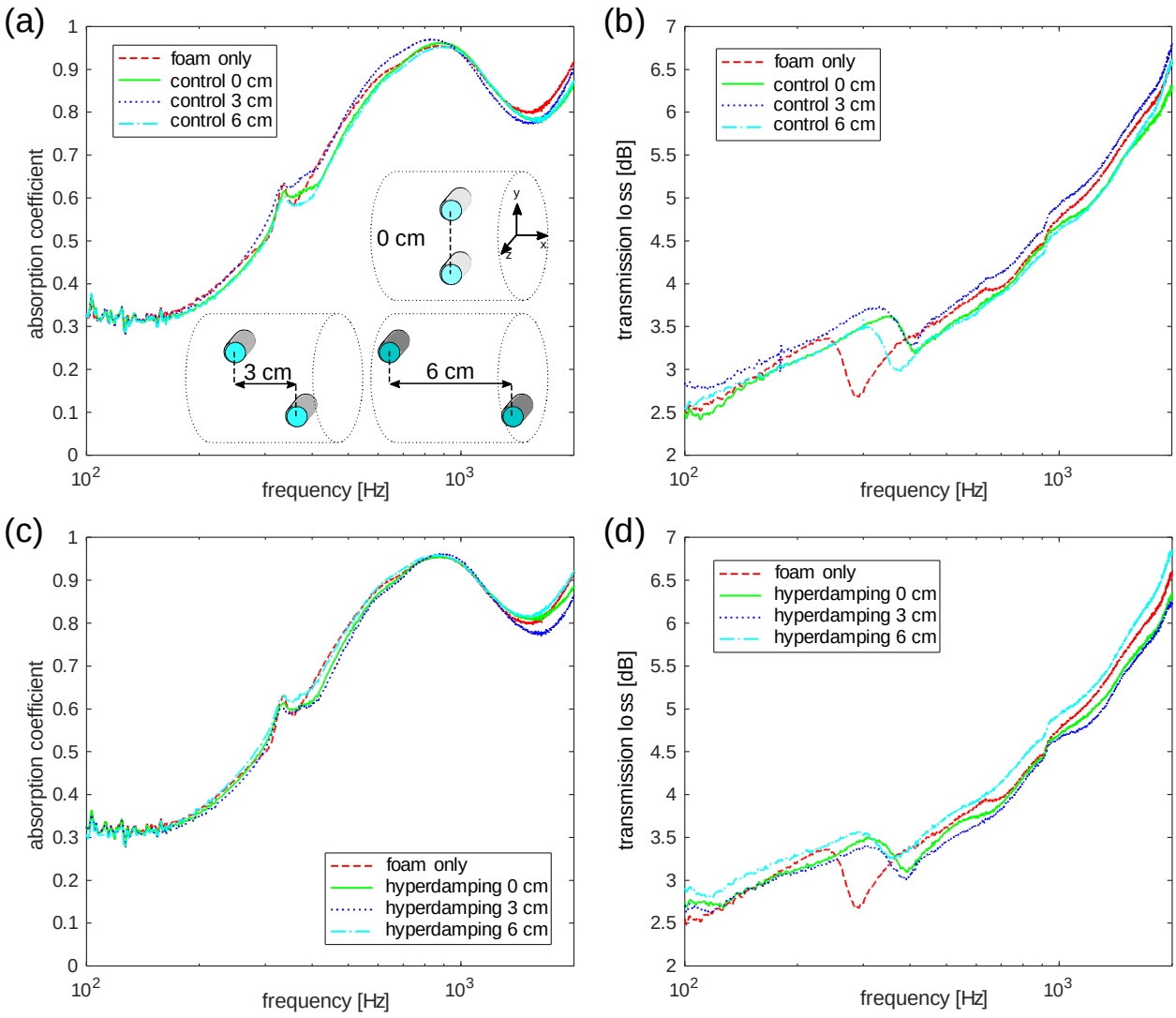

Figure 14: Changing spacing between control solid elastomer inclusions (a) absorption coefficient and (b) transmission loss; Changing spacing between hyperdamping inclusions (c) absorption coefficient and (d) transmission loss

Changing the spacing of two hyperdamping inclusions shows more influence on absorption coefficient than changing the spacing of two control solid elastomer inclusions. The 6 cm spacing is the only spacing to increase absorption coefficient broadband, while the other two spacings decrease the absorption coefficient slightly in the range of 400 Hz to 700 Hz, and above 1000 Hz. This result contrasts with the simulation, where all spacings increased the absorption coefficient. This suggests that the model does not accurately simulate the change in absorption coefficient between a pure foam specimen and a hyperdamping metamaterial specimen. However, it does follow the same trend that the increased spacing between two inclusions increases effectiveness at noise control. For transmission loss shown in (d), the 6 cm spacing is again the only spacing which is shows a broadband increase in transmission loss. However, the 0 cm and 3 cm spacing are both effective at increasing transmission loss in the range of 250 Hz to 350 Hz.

The same specimens are tested by an electrodynamic shaker for force transmissibility, which gives a much higher level of input energy compared to acoustic tests, and may cause nonlinear response. When compared to the force transmission through the poroelastic foam specimen itself, the mass from the inclusions in the metamaterial specimens causes a resonance in the region of 50 Hz to 125 Hz, yet as seen in Figure 15, the resonance changes based on the inclusion architecture and the spacing between inclusions. The resonance peak tends to occur at a higher frequency when the inclusions are spaced apart by 3cm than 6 cm, and is lowest in frequency when the inclusions are directly beside each other. From approximately 150 Hz to 500 Hz, force transmissibility tends to decrease with the addition of two inclusions. Above 500 Hz, the low-level dynamics of the force expander plates are more prominent than the dynamics of the specimens so that the force transmission associated with the specimens above 500 Hz is effectively negligible. It can be seen in Figure 14(b) that for the control solid elastomer inclusions, the 0 cm spacing decreases force transmissibility more than the other spacings in the 150 Hz to 225 Hz band, while the 6 cm spacing decreases force transmissibility more than the other spacings above 300 Hz. On the other hand, for all three hyperdamping architectures in Figure 14(d), the 0 cm and 6 cm spacing tend to have similar force transmissibilities in the 150 Hz to 225 Hz band, while the 6 cm spacing has the greatest decrease in force transmissibility above 300 Hz, which suggests that hyperdamping inclusions are more effective at reducing force transmissibility and therefore increasing energy absorption when spread out.

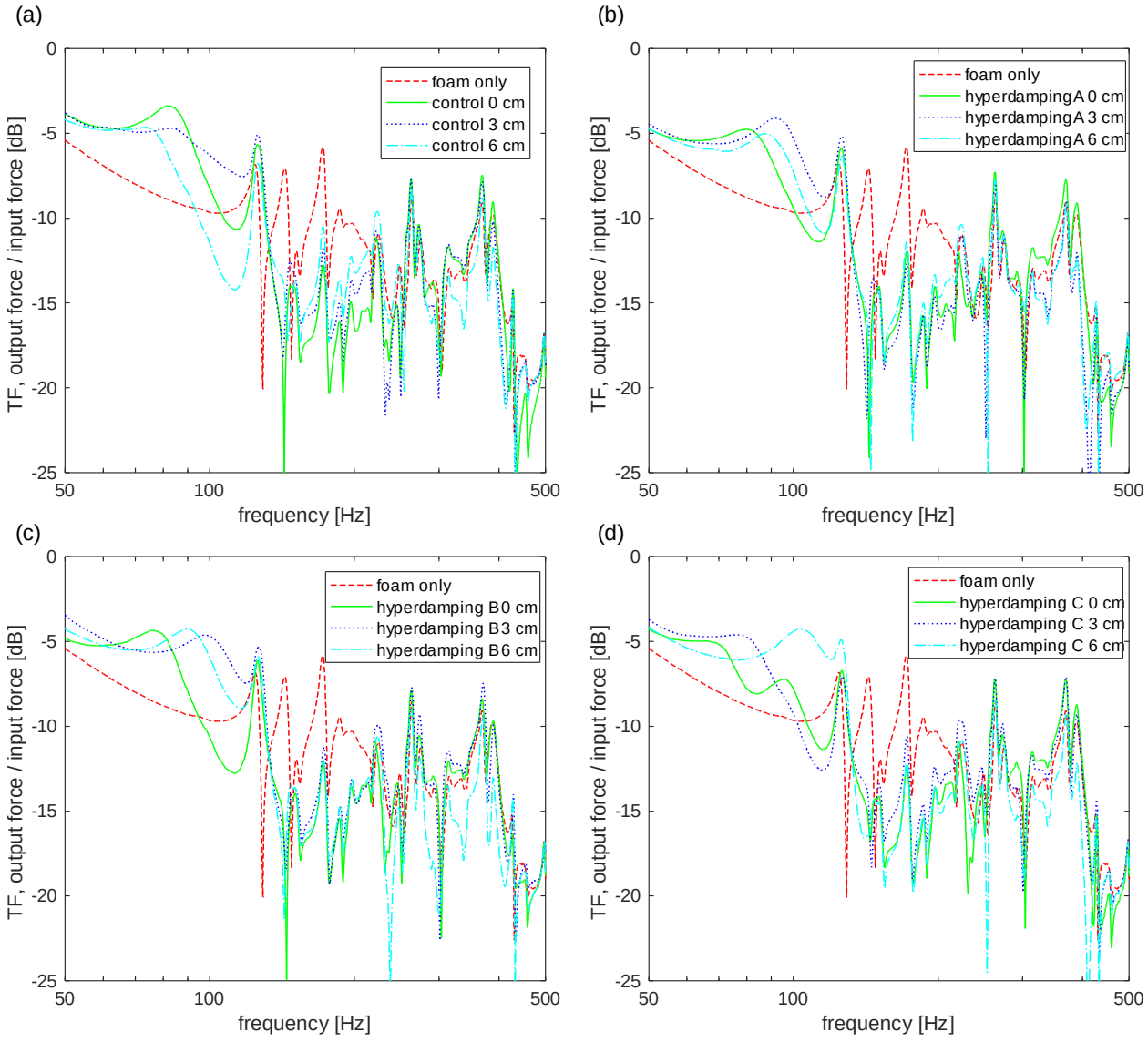

Figure 15: Force transmissibility with changing spacing for (a) control solid elastomer inclusions (b) hyperdamping architecture 1 inclusions (c) hyperdamping architecture 2 inclusions (d) hyperdamping architecture 3 inclusions

One-third octave band is a summation of a frequency response over defined frequency ranges, in order to quantify system response over defined bands. In the case of force transmissibility, this summation provides a measure of energy transmission capability over each band, so reducing the one-third octave band values corresponds to a reduction in force transmissibility and an increase in energy absorption. To quantify the resonance behavior, which is a result of the added mass, the sum of one-third octave bands from 50 Hz to 125 Hz is taken and shown in Figure 16 (a). It can be seen that between the three spacing groups, the magnitude remains around 5 to 6 dB. The same summation is performed across the attenuation band of 157 Hz to 500 Hz, in order to quantify the effectiveness of inclusions to decrease force transmission, which is seen in Figure 16 (b). The magnitudes of the 6 cm group are clearly reduced from the magnitudes of the 0

cm and 3 cm group. This reduction in cumulative one-third octave bands means that all architectures are more effective at attenuating vibrations when spread out, while the resonance is not significantly increased.

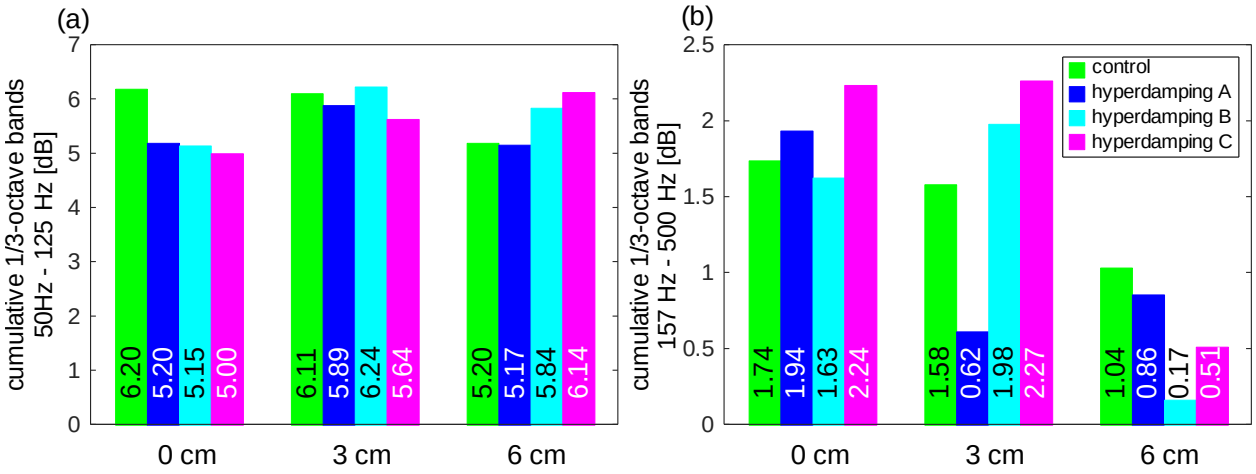

Figure 16: Cumulative one-third octave band with changing spacing in (a) resonance region of 50 Hz – 125 Hz and (b) attenuation region of 157 Hz – 500 Hz

4.2 Influence of arrangement of inclusions

To further investigate the interactions that may occur among inclusions, arrangements of 2 inclusions are considered in each of the x, y, and z direction previously defined. Guided by the fact that absorption coefficient and transmission loss are increased by hyperdamping inclusions which are spread apart, and that force transmissibility is decreased more by inclusions which are far apart, spacing between inclusions in the direction of wave propagation is 50 mm center-to-center. Spacing in the y and z directions is constrained by the size of the standing wave tube, such that the inclusions are not too close to the edge of the tube. Because of this constraint, spacing in the y and z direction is chosen to be 38 mm center-to-center, which is the maximum possible spacing.

Arrangements of two inclusions are shown in Figure 17. It is seen that absorption coefficient and transmission loss increase broadband for all arrangements, when compared to the foam baseline specimen. Both absorption coefficient and transmission loss tend to increase more for the 1x2x1 and 1x1x2 arrangements than for the 2x1x1 arrangement. This suggests that a “screen” approach would most effectively capture incoming noise. The specific architecture used has the most influence for the y direction, in both absorption coefficient and transmission loss. This is likely due to interactions between the two inclusions, which resonate primarily in the x and y direction due to their geometry.

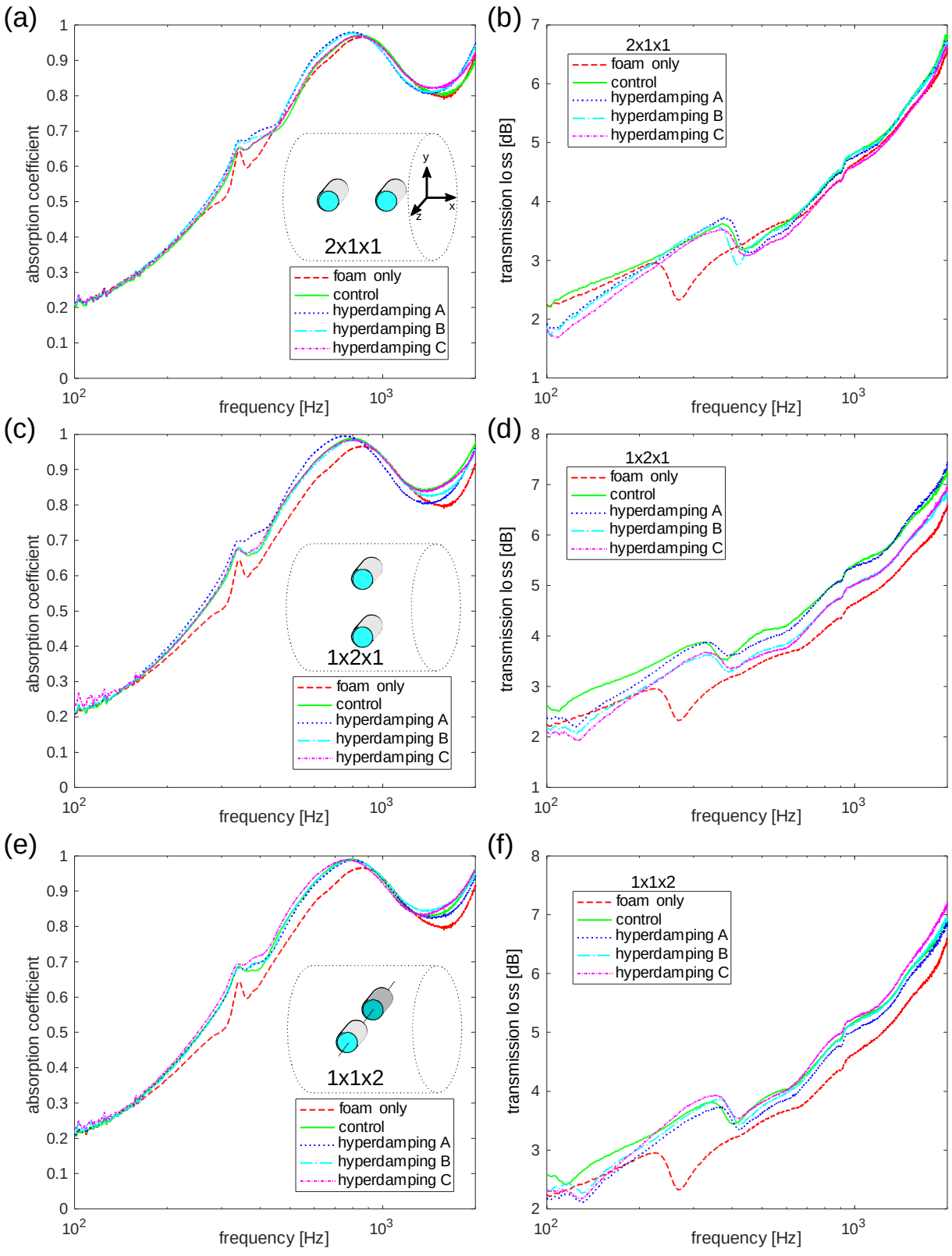

Figure 17: All architectures of 2x1x1 (a) absorption coefficient and (b) transmission loss; all architectures of 1x2x1 (c) absorption coefficient and (d) transmission loss; all architectures of 1x1x2 (e) absorption coefficient and (f) transmission loss

When comparing among the three hyperdamping architectures, where A is not buckled, B is very nearly buckled, and C is post-buckled, neither of the architectures is distinctly more effective than the others. For the 2x1x1 and 1x2x1 arrangements, architecture A increases absorption coefficient the most, but does not do the same for transmission loss. For the 1x1x2 arrangement, architecture C increases both absorption coefficient and transmission loss more than the other architectures at most frequencies. This suggests that hyperdamping is a robust phenomenon, which is effective at noise capture not just at the elastic stability limit, but also slightly before and beyond it. This is in contrast to many recent advancements in vibroacoustic energy control, which are sensitive to parameter tuning, such as multiple folding mechanisms [13].

To better quantify the influence of arrangement, the absorption coefficient and transmission loss are compared directly between arrangements for both the control solid and the hyperdamping architecture A, as seen in Figure 18. From this, it is clear that an arrangement with two inclusions in the direction of wave propagation, noted here as 2x1x1, has a broadband lower absorption coefficient and transmission loss than arrangements of two inclusions perpendicular to the direction of wave propagation. This suggests that the 2x1x1 arrangement is less effective at broadband noise capture than the 1x2x1 arrangement and the 1x1x2 arrangement. On the other hand, for the control solid inclusions, the y and z directions have similar absorption levels, with the y direction having slightly higher transmission loss than the z direction. For the hyperdamping inclusions, there is more distinction between the different arrangements of two inclusions. Interestingly, the hyperdamping arrangement of two inclusions in the direction of wave propagation appears to decrease the transmission loss at low frequencies, while the control solid elastomer inclusion does not.

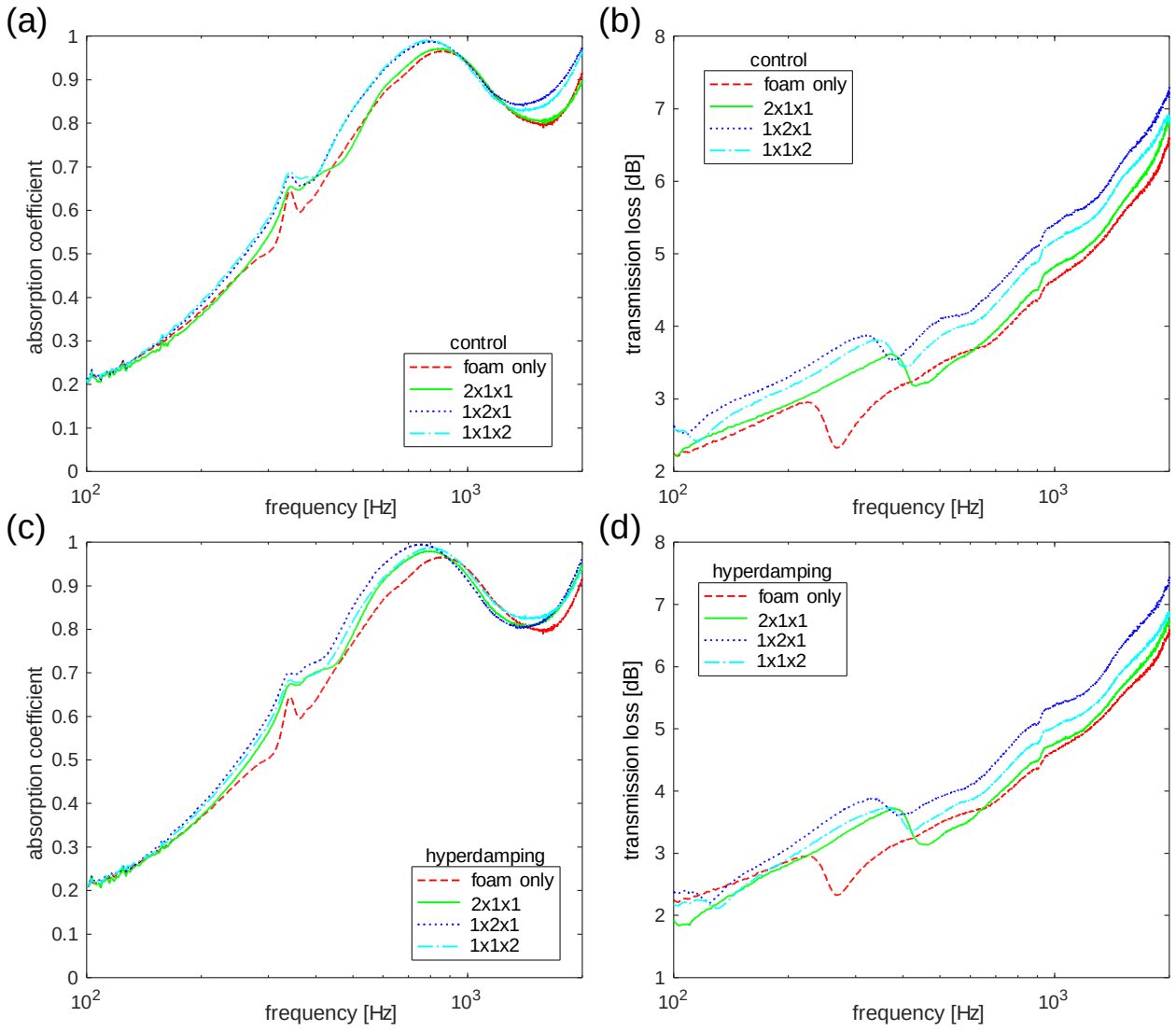

Figure 18: All arrangements of 2 control solid elastomer inclusions (a) absorption coefficient and (b) transmission loss; all arrangements of 2 hyperdamping A inclusions (c) absorption coefficient and (d) transmission loss

The specimens of varying arrangement are tested with an electrodynamic shaker to determine force transmissibility. In Figure 19, each architecture is compared for each arrangement of two inclusions. For the 2x1x1 arrangement in Figure 19 (a), the different architectures have a similar response in the attenuation band of 150 Hz to 500 Hz. The resonance occurs at about 100 Hz for all architectures, though it varies in shape and amplitude. The hyperdamping architectures all have a lower resonance amplitude, which may be in part due to their decreased mass compared to the control solid inclusions. For the 1x2x1 arrangement in Figure 19(b), there is greater change in force transmissibility between inclusion architectures in the attenuation band, and the hyperdamping architectures clearly decrease force transmissibility by more than the control solid elastomer inclusions. For the 1x1x2 arrangement in Figure 19 (c), there is less distinction between the architectures. Yet, the hyperdamping architectures are more effective than the control solid.

For both the 1x2x1 and 1x1x2 arrangements, the control solid elastomer inclusions have resonances at lower frequency than the hyperdamping inclusions, although all tend to occur at similar amplitudes, and the hyperdamping architectures share similar resonance shapes. Because the 1x2x1 and 1x1x2 arrangements have similar resonances, this resonance is most likely due to the lumped motion of the inclusions and not due to interactions between the inclusions. On the other hand, interactions between the inclusions likely do influence the resonance shape, because the 2x1x1 arrangement has a different shape, which may be due to the fact that the inclusions are spread farther apart for this arrangement.

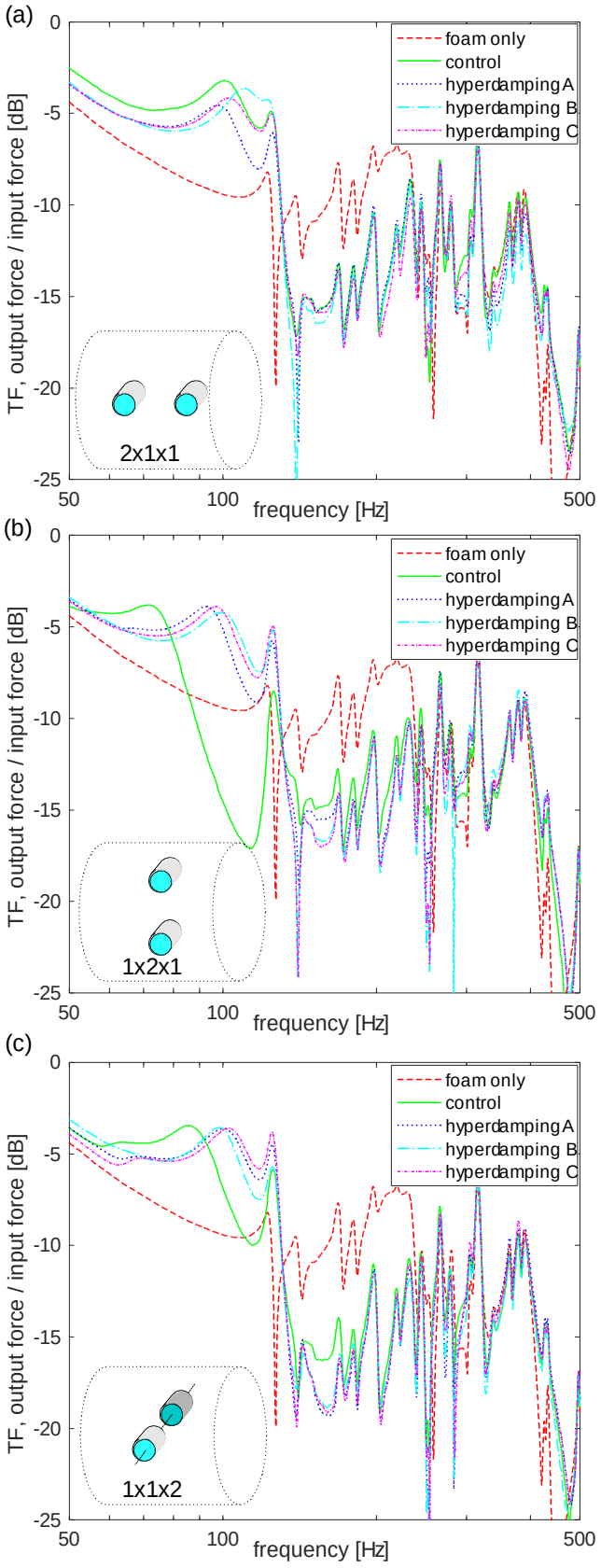

Figure 19: Force transmissibility for arrangements of 2 inclusions (a) 2x1x1, (b) 1x2x1, and (c) 1x1x2

To better compare between arrangements, arrangements are plotted together for each architecture in Figure 20. From this, it can be seen that the 1x1x2 arrangement tends to have the lowest force transmissibility across the previously defined attenuation band of 157 Hz to 500 Hz for metamaterials of all inclusion architectures. This, combined with the fact that the 1x2x1 arrangement shows more distinction between architectures than the 2x1x1 arrangement, suggests that the screen approach previously suggested may be the most effective method of attenuating both noise and vibrations. This approach would entail one layer of hyperdamping inclusions arranged in a grid. While a multi-layer grid would improve the effectiveness, it would result in diminishing returns and may also significantly increase the thickness of foam required. With this screen approach in mind, foams thinner than the 100 mm samples studied here could be utilized. Additionally, while tailoring the spacing in the z direction would have some role on the effectiveness of the metamaterial, it seems that tailoring the spacing in the y direction would have a much greater influence the capabilities of the metamaterial, due to the interactions between inclusions in this direction.

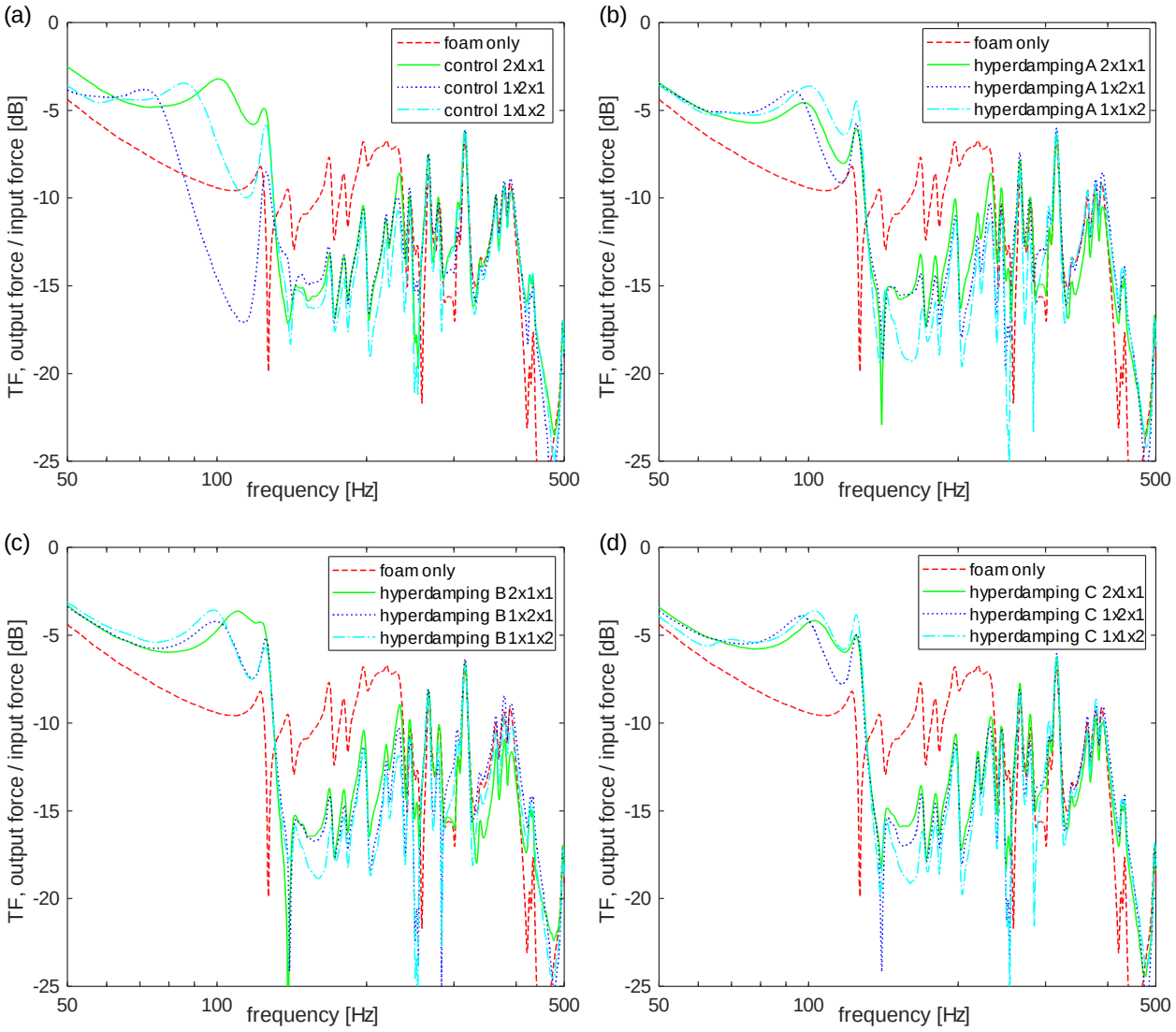

Figure 20: Force transmissibility for all arrangements of two inclusions of (a) control solid elastomer inclusions, (b) not yet buckled hyperdamping inclusions, (c) very nearly buckled hyperdamping inclusions, and (d) post-buckled hyperdamping inclusions

By taking the summation of the one-third octave bands over the resonance and attenuation bands, the performance of the inclusion arrangements can be quantified as the increase in force transmissibility over the resonance band and decrease in force transmissibility in the attenuation band, as previously defined. As shown in Figure 21, resonance energy tends to be between 6 dB and 7 dB. The magnitude is slightly lower for the 1x2x1 arrangements than the other arrangements, but because the resonances are so close in magnitude it is likely that the resonance behavior in this band is due to lumped motion of the inclusions, while the arrangement only slightly affects this behavior. On the other hand, the attenuation band clearly shows that energy is reduced the most by the 1x1x2 arrangement for all architectures of hyperdamping, and for the control solid elastomer inclusions. While the 1x2x1 arrangement showed the most distinction between different architectures, it also shows the highest cumulative one-third octave band, which is not apparent from the narrowband plots alone. While the 1x2x1 arrangement is more effective than the 2x1x1

arrangement across most frequencies, it also shows a slightly higher amplitude resonance near 375 Hz, which may be the cause of the high cumulative one-third octave band. Thus, depending on the desired frequency range of attenuation, a 2x1x1 or 1x2x1 may be better suited.

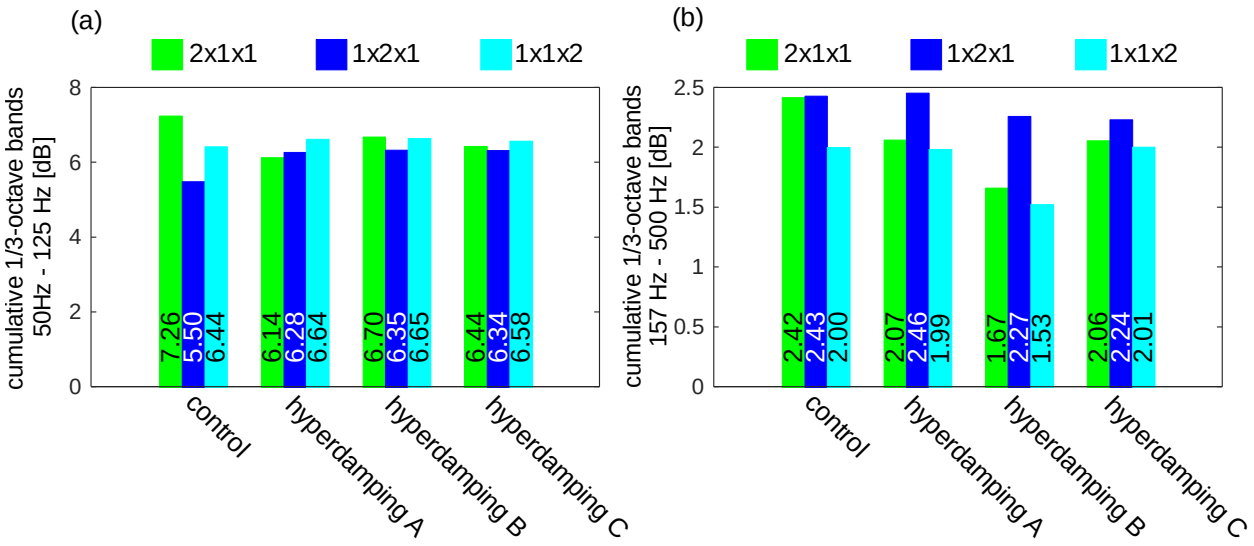

Figure 21: Cumulative one-third octave band for each arrangement of two inclusions in (a) resonance region of 50 Hz – 125 Hz and (b) attenuation region of 157 Hz – 500 Hz

Next, two arrangements of four inclusions are considered. Due to the size of the samples, only two of the possible three arrangements are considered: 2x2x1 and 2x1x2. The a 1x2x2 arrangement does not fit within the 85 mm diameter foam samples. Due to the numerous fabrication steps required to create these four inclusion samples, acoustic testing results in poor data due to the samples not seating correctly within the standing wave tube. Yet, these samples give quality force transmissibility data showing clear and consistent trends due to the differing boundary conditions between acoustic tests and shaker tests. The force transmissibility results are shown in Figure 22. From these plots, it is seen that the 2x2x1 arrangement increases the resonance amplitudes more than the 2x1x2 arrangement, yet results in more change in force transmissibility between architectures in both the resonance and attenuation bands. This again reflects the fact that inclusions interact more in the y direction, which has previously been defined as the direction perpendicular to the center axis of the shells, and perpendicular to the direction of wave propagation, than in the z direction, which is aligned with the central axis of the shells. This reinforces the previous conclusion that tailoring the spacing between inclusions in the directions of motion, namely the x and y directions in this study, will result in more change than tailoring the spacing between inclusions perpendicular to the direction of motion, namely the z direction in this study.

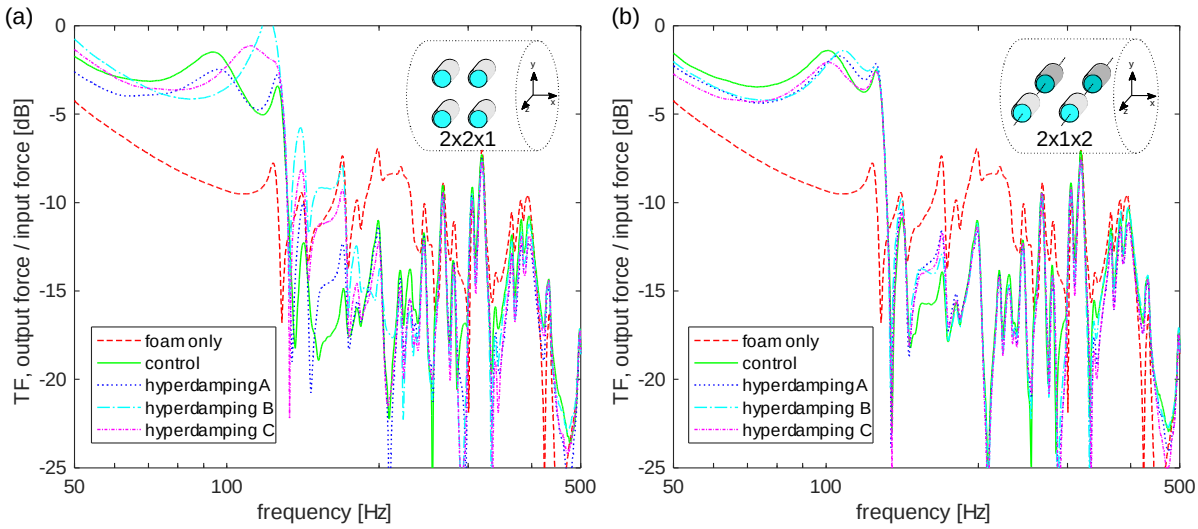

Figure 22: Force transmissibility for all architectures with four inclusions arranged as (a) 2x2x1 and (b) 2x1x2

To quantify the influence of changing the number of inclusions, one-third octave band is summed across the previously defined resonance band and attenuation band as shown in Figure 23. Unsurprisingly, as the number of inclusions increases, the resonance energy increases and the attenuation energy decreases in most cases. Interestingly, this is not true for the hyperdamping B architecture. This may be attributed in part to the fact that the hyperdamping B four inclusion arrangement had a higher frequency resonance than all other arrangements, which may have affected the lower part of the attenuation band. On the other hand, the overall results do follow the expected trends, wherein vibration attenuation can be increased in the attenuation band at the cost of an increase in the resonance band. This suggests that for situations with higher frequency inputs, utilizing more inclusions of any architecture will result in greater vibration reduction, but for purely broadband inputs, the benefit of reduced higher frequency vibrations will come with a tradeoff at lower frequencies, which must be kept in mind for each specific application.

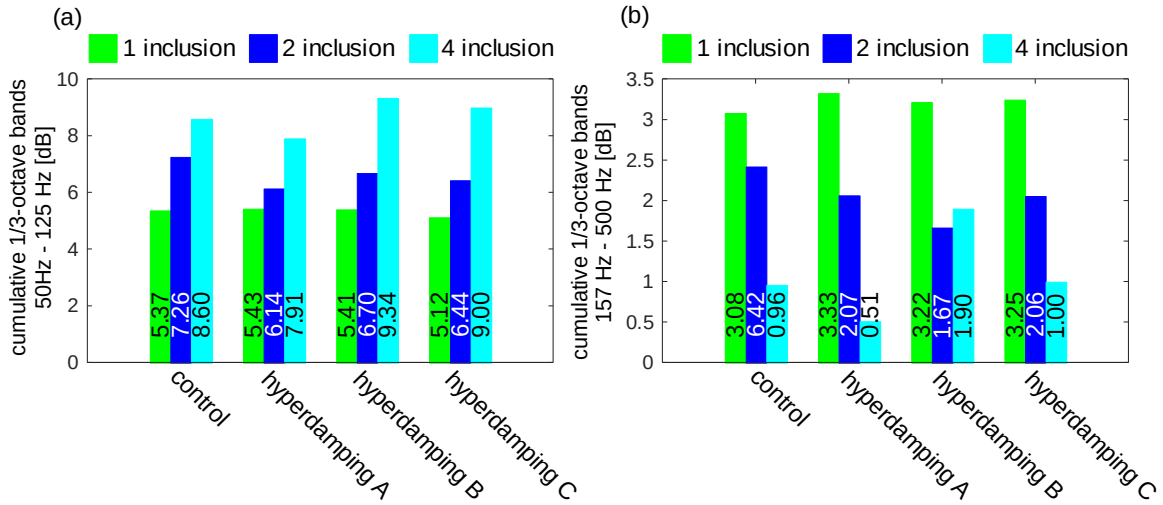

Figure 23: Cumulative one-third octave band with changing number of inclusions for each architecture in (a) resonance region of 50 Hz – 125 Hz and (b) attenuation region of 157 Hz – 500 Hz

5 CONCLUSION

Lightweight, broadband damping material systems are needed in a wide range of applications with unwanted vibrations or noise, where increasing weight comes as a penalty to application efficiency. Many traditional solutions either add significant mass, or are narrowband dampers that utilize resonance phenomena. Hyperdamping metamaterials composed of one inclusion near its elastic stability limit embedded within foam have previously been demonstrated to increases absorption and decrease force transmissibility compared to foam alone. Yet, a practical realization of hyperdamping is likely to required multiple hyperdamping inclusions arrayed with foam.

Periodically arranged hyperdamping inclusions embedded in foam are characterized for noise and vibration reduction capabilities in this research. This characterization is intended to guide the design of future hyperdamping metamaterial arrays for both spacing and arrangement of inclusions, in addition to demonstrating the robustness of hyperdamping inclusions.

Finite element models of hyperdamping metamaterials demonstrate that the inclusions are more effective at increasing acoustic absorption coefficient when spread far apart, while also demonstrating that have two inclusions perpendicular to the direction of wave propagation will be more effective than have two inclusions parallel to the direction of wave propagation. However, this model is phenomenological and thus does not accurately quantify the increase in absorption coefficient, so results must be examined qualitatively between designs.

Acoustic and vibration experiments demonstrate that hyperdamping metamaterials are more effective when inclusions are spread apart, as evidence by a broadband increase in absorption coefficient and transmission loss, and a broadband reduction in force transmissibility. This result verifies the phenomenological simulation.

Arrays of two inclusions are shown to be more effective when arranged perpendicular to the direction of wave propagation compared to being parallel to the direction of wave propagation. This suggests that a “screen” design would most effectively capture incoming noise and vibrations. This also suggests that having multiple layers of this screen would increase vibroacoustic damping, but with diminishing returns where each added layer increases the damping by less than the previous layer.

Increasing the number of inclusions is seen to decrease force transmissibility in the attenuation band, while increasing it in the resonance band, as intuition would suggest. This tradeoff must be considered when designing hyperdamping metamaterial arrays in order to determine the optimal number of inclusions to use depending on the desired bandwidth of attenuation.

Hyperdamping metamaterials are seen to be as or more effective at attenuating vibroacoustic energy for all arrangements of two inclusions, while providing such attenuation with reduced mass compared to conventional solid inclusions. Additionally, hyperdamping is shown to be robust wherein all three hyperdamping architectures perform comparably despite the architectures being intentionally fabricated so that one is not yet buckled, one is very nearly buckled, and one is post-buckled. This robustness means that

hyperdamping is not a parameter sensitive phenomenon, and can still be effective even when it is not ideally tuned.

5.1 Future Investigations

The behavior of periodically arranged hyperdamping inclusions within foam is investigated with extensive experimental studies and simulations. These findings lay a guide for the implementation of multiple hyperdamping inclusions within foam in order to increase vibroacoustic attenuation. The results may be used to guide further simulations of hyperdamping metamaterials, including a refined acoustic model to include transmission loss computation. Modeling the hyperdamping inclusions to explicitly buckle remains a challenging problem, due to the multi-level contact between air, elastomer, shell, and foam. Yet, an explicit model could predict absorption more accurately for lower frequencies, and may reduce inconsistencies between simulation and experiment. Additionally, it could be utilized to model force transmissibility of a harmonically excited specimen, which is not possible with a phenomenological model.

The major limitation for studies of a higher number of inclusion is the diameter of the standing wave tube used for acoustic measurements. While standing wave tubes are a convenient tool for small samples, larger samples are often tested in anechoic-reverberant transmission loss suites. The use of an anechoic-reverberant chamber would allow much larger samples with more inclusions embedded within, in order to expand on the concept of a screen approach of energy capture using hyperdamping inclusions.

While this study used a rotationally symmetric hyperdamping inclusion geometry with 7 voids, further studies may characterize a more optimal geometry to further decrease inclusion mass while increasing vibroacoustic attenuation beyond what has already been achieved. Additionally, the size of the inclusions used in this study presented challenges due to the size of the standing wave tube used. Fabrication of smaller inclusions has not yet been realized due to the limitations of the current fabrication method. Yet, smaller inclusions distributed more closely together may prove to be an effective method of energy capture.

REFERENCES

[1] E. Baravelli and M. Ruzzene, "Internally resonating lattices for bandgap generation and low-frequency vibration control," *Journal of Sound and Vibration,* vol. 332, pp. 6562-6579, 2013.

[2] J. Allard and N. Atalla, Propagation of Sound in Porous Media: Modelling Sound Absorbing Materials, Chichester: John Wiley and Sons, 2009.

[3] L. Cremer, M. Heckl and B. Petersson, Structure-Borne Sound: Structural Vibrations and Sound Radiation at Audio Frequencies, Berlin: Springer, 2005.

[4] D. Bies and C. Hansen, Engineering Noise Control: Theory and Practice, London: Spon Press, 2006.

[5] T. Sain, J. Meaud, G. Hulbert, E. Arruda and A. Waas, "Simultaneously high stiffness and damping in a class of wavy composites," *Composite Structures,* vol. 101, pp. 104-110, 2013.

[6] M. Nouh, O. Aldraihem and A. Baz, "Wave propagation in metamaterial plates with periodic local resonances," *Journal of Sound and Vibration,* vol. 341, pp. 53-73, 2015.

[7] I. Antoniadis, D. Chronopoulos, V. Spitas and D. Koulocheris, "Hyper-damping peroperties of a stiff and stable linear oscillator with a negative stiffness element," *Journal of Sound and Vibration,* vol. 346, pp. 37-52, 2015.

[8] L. Dong and R. Lakes, "Advanced damper with negative structural stiffness elements," *Smart Materials and Structures,* vol. 21, p. 075026, 2012.

[9] X. Liu, G. Hu, G. Huang and C. Sun, "An elastic metamaterial with simultaneously negative mass density and bulk modulus," *Applied Physics Letters,* vol. 98, p. 251907, 2011.

[10] D. Restrepo, N. Mankame and P. Zavattieri, "Phase transforming cellular materials," *Extreme Mechanics Letters,* vol. 4, pp. 52-60, 2015.

[11] P. Wang, F. Casadei, S. Shan, J. Weaver and K. Bertoldi, "Harnessing buckling to design tunable locally resonant acoustic metamaterials," *Physical Review Letters,* vol. 113, p. 014301, 2014.

[12] S. Shan, S. Kang, J. Raney, P. Wang, L. Fang, F. Candido, J. Lewis and K. Bertoldi, "Multistable architected materials for trapping elastic strain energy," *Advanced Materials,* vol. 27, pp. 4296-4301, 2015.

[13] S. Shan, S. Kang, P. Wang, C. Qu, S. Shian, E. Chen and K. Bertoldi, "Harnessing multiple folding mechanisms in soft periodic structures for tunable control of elastic waves," *Advanced Functional Materials,* vol. 24, pp. 4935-4942, 2014.

[14] B. Florijn, C. Coulais and M. van Hecke, "Programmable mechanical metamaterials," *Physical Review Letters,* vol. 113, p. 175503, 2014.

[15] N. Hu and R. Burgueño, "Buckling-induced smart applications: recent advances and trends," *Smart Materials and Structures,* vol. 24, p. 063001, 2015.

[16] Z. Bažant and L. Cedolin, Stability of Structures: Elastic, Inelastic, Fracture, and Damage Theories, Hackensack, New Jersey: World Scientific Publishing Co., 2010.

[17] L. Virgin and R. Wiebe, "On damping in the vicinity of critical points," *Philosophical Transactions of the Royal Society A,* vol. 371, p. 20120426, 2013.

[18] D. Inman, Engineering Vibration, Saddle River, New Jersey: Prentice Hall, 2001.

[19] J. Bishop, Q. Dai, Y. Song and R. Harne, "Resilience to impact by extreme energy absorption in lightweight material inclusions constrained near a critical point," *Advanced Engineering Materials,* vol. 18, pp. 1871-1876, 2016.

[20] R. Harne, Y. Song and Q. Dai, "Trapping and attenuating broadband vibroacoustic energy with hyperdamping metamaterials," *Extreme Mechanics Letters,* vol. 12, pp. 41-47, 2017.

[21] C. Fuller and R. Harne, "Passive distributed vibration absorbers for low frequency noise control," *Noise Control Engineering Journal,* vol. 58, pp. 627-635, 2010.

[22] K. Idrisi, M. Johnson, D. Theurich and J. Carneal, "A study on the characteristic behavior of mass inclusions added to a poro-elastic layer," *Journal of Sound and Vibration,* vol. 329, pp. 4136-4148, 2010.

[23] A. Slagle and C. Fuller, "Low frequency noise reduction using poro-elastic acoustic metamaterials," in *Proceedings of the 21st AIAA/CEAS Aeroacoustics Conference,* Dallas, Texas, USA, 2015.

[24] K. Idrisi, M. Johnson, A. Toso and J. Carneal, "Increase in transmission loss of a double panel system by addition of mass inclusions to a poro-elastic layer: a comparison between theory and experiment," *Journal of Sound and Vibration,* vol. 323, pp. 51-66, 2009.

[25] R. Harne and C. Fuller, "Lightweight distributed vibration absorbers for marine structures," *Proceedings of Meetings on Acoustics,* vol. 9, p. 065003, 2010.

[26] O. Doutres and N. Atalla, "Transfer matrix modeling and experimental validation of cellular porous material with resonant inclusions," *The Journal of the Acoustical Society of America,* vol. 137, pp. 3502-3513, June 2015.

[27] C. Lagarrigue, J. Groby, V. Tournat, O. Dazel and O. Umnova, "Absorption of sound by porous layers with embedded periodic arrays of resonant inclusions," *The Journal of the Acoustical Society of America,* vol. 134, pp. 4670-4680, 2013.

[28] J. Groby, C. Lagarrigue, B. Brouard, O. Dazel and V. Tournat, "Using simple shape three-dimensional rigid inclusions to enhance porous layer absorption," *The Journal of the Acoustical Society of America,* vol. 136, pp. 1139-1148, 2014.

[29] ASTM International, "Standard Test Method for Impedance and Absorption of Acoustical Materials Using a Tube, Two Microphones and a Digital Frequency Analysis System," 2012.

[30] R. Panneton and X. Olny, "Acoustical determination of the parameters governing viscous dissipation in porous media," *The Journal of the Acoustical Society of America,* vol. 119, pp. 2027-2040, 2006.

[31] The Foam Factory, "Product general and technical information".

[32] ASTM International, "Standard Test Method for Measurement of Normal Incidence Sound Transmission of Acoustical Materials Based on the Transfer Matrix Method," 2009.

[33] A. Barnard and M. Rao, "Measurement of sound transmission loss using a modified four microphone impedance tube," in *NOISE-CON*, Baltimore, MD, 2004.

[34] J. Plattenburg, "Design, analysis, and evaluation of impedance tube with experimental characterization of acoustic materials," 2013.

6 APPENDIX

6.1 Sample absorption coefficient MATLAB code

```
%% data acquisition toolbox NI
clear all
warning off

%% acquire data?
dataacquire=1; % yes for acquire

%% experimental setup parameters
d.test_name='10323d_067r_2x1x1'; % specimen label

%% impedance tube parameters
d.mic_spacing=3*.0254; % m
d.mic_dist=3.5*.0254; % m
d.temp= (72-32)/1.8; % room temperature in Celsius
d.press=101.325e3; % pressure Pa
d.cspeed=20.047*sqrt(273.15+d.temp); % m/s speed of sound in room

%% data acquisition setup parameters
d.fs=65536; % sampling frequency [Hz]
d.wind=@hann; % window type for averages
d.seconds=40; % [s] seconds of data acquisition,
d.filter_data_lo=40; % [Hz] of low pass cut off frequency
d.filter_data_hi=3000; % [Hz] of high pass cut off frequency
%% fft computation parameters
d.time_sampled_per_fft=1; % [s] seconds of data acquisition over which fft is
evaluated
d.spacing_cts=round(d.fs*d.time_sampled_per_fft); % number of samples to use
in FFT to obtain freq_spacing
d.fft_numbers=floor(d.fs*d.seconds/d.spacing_cts); % number of ffts to
compute/loop through
d.nft=2^nextpow2(d.spacing_cts); % number of samples next to power of 2 for
spacing_cts

%% filename for save d structure
c=clock; % grab the time-stamp, eliminates possibility of data overwrite
d.filename=[num2str(c(1)) '_' num2str(c(2),'%02.0f') '_'
num2str(c(3),'%02.0f') '_' num2str(c(4),'%02.0f') num2str(c(5),'%02.0f')
'_impedance_tube_' d.test_name '.mat'];
saveon=1; % save the data?

%% sensor sensitivity
d.sensor{1}='PCB_130E20_SN_43104_microphone';
d.sensor{2}='PCB_130E20_SN_43105_microphone';
d.ch_sens(1)=1/0.030871; % [Pa] from 1/[mV/Pa] % PCB_130E20_SN_43104
Microphone
d.ch_sens(2)=1/0.028170; % [Pa] from 1/[mV/Pa] % PCB_130E20_SN_43105
Microphone

%% mean sensor values [V] for each channel, to be subtracted from the input
before sensitivity to [units]
d.data_mean(1)=0; % mean PCB_130E20_SN_43104 Microphone voltage [V]
```

```
d.data_mean(2)=0; % mean PCB_130E20_SN_43105 Microphone voltage [V]

%% if for data acquisition
if dataacquire==1 % 1=yes for acquire

%% identify connected devices
devices=daq.getDevices;
% once obtained, ensure using correct device name in below session and
acquire lines

%% acquire data
s=daq.createSession('ni');
s.addAnalogInputChannel('Dev1',0,'Voltage'); % add input channels
s.addAnalogInputChannel('Dev1',1,'Voltage');
s.Rate=d.fs; % set output and measuring frequency [Hz]
s.DurationInSeconds=d.seconds; % [s] duration of data acquisition
[d.data,d.time_series]=s.startForeground;
d.nn_chan=min(size(d.data));

%% bandpass filter data
clear ch_f
d.nn_chan=min(size(d.data));
%
myfilt=designfilt('lowpassiir','filterorder',4,'passbandfrequency',d.filter_d
ata_hi,'PassbandRipple',0.01,'samplerate',d.fs);
myfilt=designfilt('bandpassiir','filterorder',4,'HalfPowerFrequency1',d.filte
r_data_lo,'HalfPowerFrequency2',d.filter_data_hi,'samplerate',d.fs);
for iii=1:d.nn_chan
ch_f(:,iii)=filtfilt(myfilt,d.ch_sens(iii)*(d.data(:,iii)-d.data_mean(iii)));
%
end

%%
end

%%
d.data_filt=ch_f; % re-assign filtered data from local to structure variable
%% post-process data
% post-processing results for noise


% load calibration data for transfer functions due to microphone variations

load('calibrate_Hca_12_09.mat');
d.Hca=Hca;

clear ch_ft gxy gxx coh tf y
d.inst_mean=[];d.f_ft=[];d.ch_ft_a=[];d.gxx_a=[];d.gxy_a=[];d.coh_a=[];d.tf_a
=[];
for ooo=1:2*d.fft_numbers-1 %  1:d.fft_numbers for no overlap.
1:2*d.fft_numbers-1 with half-overlap as defined below in trunc
    trunc=(ooo-1)*d.spacing_cts/2+1:ooo*d.spacing_cts/2+d.spacing_cts/2; %
define truncation in time : gives half-overlap of windowed averages is the
ooo=1:2*d.fft_numbers-1
    for iii=1:d.nn_chan
```

```
    d.inst_mean(ooo,iii)=mean(d.data_filt(trunc,iii)); % mean of
instantaneous data stream for the channel

y(:,iii)=fft(d.data_filt(trunc,iii).*window(d.wind,length(trunc)),d.nft)/(d.s
pacing_cts*mean(window(d.wind,length(trunc))));
    ch_ft(:,iii,ooo)=2*abs(y(1:d.nft/2+1,iii)); % magnitude of single-sided
fourier transform
    gxx(:,iii,ooo)=y(:,iii).*conj(y(:,iii)); % auto power spectrum
    if iii>0
    gxy(:,iii,ooo)=y(:,1).*conj(y(:,iii)); % cross power spectrum,
referencing input force
    end
    end

end

for iii=1:d.nn_chan
d.ch_ft_a(:,iii)=mean(squeeze(ch_ft(1:d.nft/2+1,iii,:)),2); % average fft of
signal
d.gxx_a(:,iii)=mean(squeeze(gxx(1:d.nft/2+1,iii,:)),2); % average
autospectrum of signal
d.gxy_a(:,iii)=mean(squeeze(gxy(1:d.nft/2+1,iii,:)),2); % average
autospectrum of signal
end

d.gxy_a=d.gxy_a(:,2); % only retain the cross-spectrum for the second channel
d.tf_a=d.gxy_a./d.gxx_a(:,1)./d.Hca; % transfer function after calibration
% d.tf_a=d.gxy_a./d.gxx_a(:,1); % transfer function before calibration
d.coh_a=abs(d.gxy_a).^2./d.gxx_a(:,1)./d.gxx_a(:,2); %coherence for the
standard and switched configurations

d.f_ft=d.fs/2*linspace(0,1,size(d.ch_ft_a,1))';

% reflection coefficient, specific acoustic impedance, absorption coefficient
d.reflect_coef=(d.tf_a-exp(j*2*pi*d.f_ft/d.cspeed*d.mic_spacing))./(exp(-
j*2*pi*d.f_ft/d.cspeed*d.mic_spacing)-d.tf_a).*exp(-
j*2*2*pi*d.f_ft/d.cspeed*(d.mic_spacing+d.mic_dist)); % reflection
coefficient
d.spec_imp=(1+d.reflect_coef)./(1-d.reflect_coef); % specific acoustic
impedance
d.absorp_coef=1-abs(d.reflect_coef).^2; % absorption coefficient

%% save data
if saveon==1
    d.data_filt=[];
    d.inst_mean=[];
    d.meansq=[];
    d.corr=[];
    d.lags=[];
    d.tf_here_est=[];
    d.tf_here_gxy=[];
    % drop original data and time series to reduce file size
    d.data=[];
    d.time_series=[];
    save(d.filename,'d');
end
```

```
%% octave and one-third octave bands

ob=1e3*2.^[-6:4]; % octave band center frequencies [Hz]
ob_lo=ob./2.^(1/2); % octave band center frequency lower [Hz]
ob_hi=ob.*2.^(1/2); % octave band center frequency higher [Hz]
otob=1e3*2.^([-18:12]/3); % one-third octave band center frequencies [Hz]
otob_lo=otob./2.^(1/6); % one-third octave center frequency lower [Hz]
otob_hi=otob.*2.^(1/6); % one-third octave center frequency higher [Hz]

% determine octave and one-third octave band absorption coefficients
% octave band
for jjj=1:length(ob)
ind1=max(find(d.f_ft<=ob_lo(jjj)));
ind2=max(find(d.f_ft<=ob_hi(jjj)));
ac_ob(jjj)=1/(ind2-ind1+1)*sum(d.absorp_coef(ind1:ind2));
end
% one-third octave band
for jjj=1:length(otob)
ind1=max(find(d.f_ft<=otob_lo(jjj)));
ind2=max(find(d.f_ft<=otob_hi(jjj)));
ac_otob(jjj)=1/(ind2-ind1+1)*sum(d.absorp_coef(ind1:ind2));
end
```

6.2 Sample transmission loss MATLAB code

```
%% data acquisition toolbox NI
clear all

warning off
%% DAT
% post-processing for transmission loss tube
% measure the transmission coefficient and transmission loss under noise
%% acquire data?
dataacquire=1; % yes for acquire
%% experimental setup parameters
d.test_name='10547_A6'; % name the file with specimen tested

% note: for 2load method, run open end first (remember to clear),after the
test, do not 'clear', and then run the anechoic termination;
% and remember to comment out the 'clear all' on top of the code
d.twoload=1; % 2 load method, 1 for anechoic termination, 2 for open end

%% filename for save d structure
c=clock; % grab the time-stamp, eliminates possibility of data overwrite
d.filename=[num2str(c(1)) '_' num2str(c(2),'%02.0f') '_'
num2str(c(3),'%02.0f') '_' num2str(c(4),'%02.0f') num2str(c(5),'%02.0f')
'_transmission_loss_tube_' d.test_name '.mat'];
saveon=1; % save the data?
%% transmission loss tube and specimen parameters
d.mic_spacing_1=3*.0254; % [m] distance between two microphones on the
speaker side
d.mic_spacing_2=3*.0254; % [m] distance between two microphones on the
termination side
d.mic_dist_1=3.5*.0254; % [m] distance from specimen's front surface (closer
to speaker) to the nearest microphone on speaker side
d.mic_dist_2=(10.5 + 5)*.0254; % [m] distance from specimen's front
surface(closer to speaker) to the nearest microphone on termination side

d.temp=(72-32)/1.8; % [celcius] room temperature
d.press=101.325e3; % pressure [Pa]
d.rho=1.290*(d.press/1000/101.325)*(273.15/(273.15+d.temp)); % [kg/m^3] air
density
d.cspeed=20.047*sqrt(273.15+d.temp); % [m/s] speed of sound in room
d.spec_thick=.101; % [m] thickness of the specimen

%% data acquisition setup parameters
d.fs=65536; % [Hz] sampling frequency
d.wind=@hann; % window type for averages
d.seconds=40; % [s] seconds of data acquisition
d.filter_data_lo=40; % [Hz] of low pass cut off frequency
d.filter_data_hi=3000; % [Hz] of high pass cut off frequency

%% fft computation parameters
d.time_sampled_per_fft=1; % [s] seconds of data acquisition over which fft is
evaluated
d.spacing_cts=round(d.fs*d.time_sampled_per_fft); % number of samples to use
in fft to obtain freq_spacing
d.fft_numbers=floor(d.fs*d.seconds/d.spacing_cts); % number of ffts to
compute/loop through
```

```
d.nft=2^nextpow2(d.spacing_cts); % number of samples next to power of 2 for
spacing_cts

%% sensor sensitivity
d.sensor{1}='PCB_130E20_SN_43104';
d.sensor{2}='PCB_130E20_SN_43105';
d.sensor{3}='PCB_130E20_SN_43101';
d.sensor{4}='PCB_130E20_SN_43102';
d.sensor{5}='loudspeaker_reference';
d.ch_sens(1)=1/0.030871; % [Pa] from 1/[mV/Pa] % PCB_130E20_SN_43104
Microphone
d.ch_sens(2)=1/0.028170; % [Pa] from 1/[mV/Pa] % PCB_130E20_SN_43105
Microphone
d.ch_sens(3)=1/0.029931; % [Pa] from 1/[mV/Pa] % PCB_130E20_SN_43101
Microphone
d.ch_sens(4)=1/0.028522; % [Pa] from 1/[mV/Pa] % PCB_130E20_SN_43102
Microphone
d.ch_sens(5)=1; % [V] reference loudspeaker

%% mean sensor values [V] for each channel, to be subtracted from the input
before sensitivity to [Pa]
d.data_mean(1)=0; % mean PCB_130E20_SN_43104 Microphone voltage[V]
d.data_mean(2)=0; % mean PCB_130E20_SN_43105 Microphone voltage[V]
d.data_mean(3)=0; % mean PCB_130E20_SN_43101 Microphone voltage[V]
d.data_mean(4)=0; % mean PCB_130E20_SN_43102 Microphone voltage[V]
d.data_mean(5)=0; % mean reference loudspeaker voltage [V]

%% if for data acquisition
if dataacquire==1 % 1=yes for acquire

%% identify connected devices
devices=daq.getDevices;
% once obtained, ensure using correct device name in below session and
acquire lines

%% acquire data
s=daq.createSession('ni');
s.addAnalogInputChannel('Dev1',0,'Voltage'); % add input channels
s.addAnalogInputChannel('Dev1',1,'Voltage');
s.addAnalogInputChannel('Dev1',2,'Voltage');
s.addAnalogInputChannel('Dev1',3,'Voltage');
s.addAnalogInputChannel('Dev1',4,'Voltage');
s.Rate=d.fs; % set output and measuring frequency [Hz]
s.DurationInSeconds=d.seconds; % [s] duration of data acquisition
[d.data,d.time_series]=s.startForeground;
d.nn_chan=min(size(d.data));

%% bandpass filter data
clear ch_f
myfilt=designfilt('bandpassiir','filterorder',4,'HalfPowerFrequency1',d.filte
r_data_lo,'HalfPowerFrequency2',d.filter_data_hi,'samplerate',d.fs);
for iii=1:d.nn_chan
ch_f(:,iii)=filtfilt(myfilt,d.ch_sens(iii)*(d.data(:,iii)-d.data_mean(iii)));
end
```

```
%%
end

%%
d.data_filt=ch_f; % re-assign filtered data from local to structure variable

%% post-process data
clear ch_ft gxy gxx coh tf y
d.inst_mean=[];d.f_ft=[];d.ch_ft_a=[];d.gxx_a=[];d.gxy_a=[];d.coh_a=[];d.tf_a
=[];
for ooo=1:2*d.fft_numbers-1 %  1:d.fft_numbers for no overlap.
1:2*d.fft_numbers-1 with half-overlap as defined below in trunc
    trunc=(ooo-1)*d.spacing_cts/2+1:ooo*d.spacing_cts/2+d.spacing_cts/2; %
define truncation in time : gives half-overlap of windowed averages is the
ooo=1:2*d.fft_numbers-1
    for iii=[5 1 2 3 4]%1:d.nn_chan
    d.inst_mean(ooo,iii)=mean(d.data_filt(trunc,iii)); % mean of
instantaneous data stream for the channel

y(:,iii)=fft(d.data_filt(trunc,iii).*window(d.wind,length(trunc)),d.nft)/(d.s
pacing_cts*mean(window(d.wind,length(trunc))));
    ch_ft(:,iii,ooo)=2*abs(y(1:d.nft/2+1,iii)); % magnitude of single-sided
fourier transform
    gxx(:,iii,ooo)=y(:,iii).*conj(y(:,iii)); % auto power spectrum
    if iii>0
    gxy(:,iii,ooo)=y(:,iii).*conj(y(:,5)); % cross power spectrum
    end
    end

end

for iii=[5 1 2 3 4]%1:d.nn_chan
d.ch_ft_a(:,iii)=mean(squeeze(ch_ft(1:d.nft/2+1,iii,:)),2); % average fft of
signal
d.gxx_a(:,iii)=mean(squeeze(gxx(1:d.nft/2+1,iii,:)),2); % average auto-
spectrum of signal
d.gxy_a(:,iii)=mean(squeeze(gxy(1:d.nft/2+1,iii,:)),2); % average cross-
spectrum of signal
d.tf_a(:,iii)=d.gxy_a(:,iii)./d.gxx_a(:,5); % transfer function before
calibration
d.coh_a(:,iii)=abs(d.gxy_a(:,iii)).^2./abs(d.gxx_a(:,5))./abs(d.gxx_a(:,iii))
; % coherence for the standard and switched configuration
end

d.f_ft=d.fs/2*linspace(0,1,size(d.ch_ft_a,1))'; % redefine frequency vector

%% complex pressure amplitude from bloton measurement eq (19)
% x1,x2,x3,x4 according to bolton measurement's Fig.1
d.x1=-(d.mic_dist_1+d.mic_spacing_1);
d.x2=-d.mic_dist_1;
d.x3=d.mic_dist_2;
d.x4=d.mic_dist_2+d.mic_spacing_2;

d.k=2*pi*d.f_ft/d.cspeed; % wave number
```

```
% complex pressure amplitude for positive, upstream direction
d.pre_amp_A=d.gxx_a(:,5).^(1/2)*j.*(d.tf_a(:,1).*exp(j*d.k*d.x2)-
d.tf_a(:,2).*exp(j*d.k*d.x1))./(2*sin(d.k*(d.x1-d.x2)));

% complex pressure amplitude for negative, upstream direction
d.pre_amp_B=d.gxx_a(:,5).^(1/2)*j.*(d.tf_a(:,2).*exp(-j*d.k*d.x1)-
d.tf_a(:,1).*exp(-j*d.k*d.x2))./(2*sin(d.k*(d.x1-d.x2)));

% complex pressure amplitude for positive, downstream direction
d.pre_amp_C=d.gxx_a(:,5).^(1/2)*j.*(d.tf_a(:,3).*exp(j*d.k*d.x4)-
d.tf_a(:,4).*exp(j*d.k*d.x3))./(2*sin(d.k*(d.x3-d.x4)));

% complex pressure amplitude for negative, downstream direction
d.pre_amp_D=d.gxx_a(:,5).^(1/2)*j.*(d.tf_a(:,4).*exp(-j*d.k*d.x3)-
d.tf_a(:,3).*exp(-j*d.k*d.x4))./(2*sin(d.k*(d.x3-d.x4)));

% acoustic pressure and particle velocity on both sides of specimen
d.pre_x0=d.pre_amp_A+d.pre_amp_B; % acoustic pressure on front surface(closer
to speaker) of specimen
d.pre_xd=d.pre_amp_C.*exp(-
j*d.k*d.spec_thick)+d.pre_amp_D.*exp(j*d.k*d.spec_thick); % acoustic pressure
on back surface (closer to termination) of specimen
d.par_vel_x0=(d.pre_amp_A-d.pre_amp_B)/d.rho/d.cspeed; % particle velocity on
front surface (closer to speaker) of specimen
d.par_vel_xd=(d.pre_amp_C.*exp(-j*d.k*d.spec_thick)-
d.pre_amp_D.*exp(j*d.k*d.spec_thick))/d.rho/d.cspeed; % particle velocity on
back surface (closer to termination) of specimen

%% transfer matrix for 1 load method
if d.oneload==1
    % elements of transfer matrix, see E2611-09 eq (24)

d.tr_ma_11=(d.pre_xd.*d.par_vel_xd+d.pre_x0.*d.par_vel_x0)./(d.pre_x0.*d.par_
vel_xd+d.pre_xd.*d.par_vel_x0); % T11
    d.tr_ma_12=(d.pre_x0.^2-
d.pre_xd.^2)./(d.pre_x0.*d.par_vel_xd+d.pre_xd.*d.par_vel_x0); % T12
    d.tr_ma_21=(d.par_vel_x0.^2-
d.par_vel_xd.^2)./(d.pre_x0.*d.par_vel_xd+d.pre_xd.*d.par_vel_x0); % T21
    d.tr_ma_22=d.tr_ma_11; % T22=T11
else
    %% pressure and particle velocity for 2 load method
    if d.twoload==1
        d.p0_a=d.pre_x0;
        d.pd_a=d.pre_xd;
        d.u0_a=d.par_vel_x0;
        d.ud_a=d.par_vel_xd;
        d.p0_b=p0_b;
        d.pd_b=pd_b;
        d.u0_b=u0_b;
        d.ud_b=ud_b;

    else
        p0_b=d.pre_x0;
        pd_b=d.pre_xd;
        u0_b=d.par_vel_x0;
        ud_b=d.par_vel_xd;
```

```
    end
% transfer matrix for 2 load method
d.denom=d.pd_a.*d.ud_b-d.pd_b.*d.ud_a;
d.tr_ma_11=(d.p0_a.*d.ud_b-d.p0_b.*d.ud_a)./d.denom;
d.tr_ma_12=(d.p0_b.*d.pd_a-d.p0_a.*d.pd_b)./d.denom;
d.tr_ma_21=(d.u0_a.*d.ud_b-d.u0_b.*d.ud_a)./d.denom;
d.tr_ma_22=(d.pd_a.*d.u0_b-d.pd_b.*d.u0_a)./d.denom;
end

%% calculation of acoustic properties
% transmission coefficient, transmission loss
d.trans_coef=2*exp(j*d.k*d.spec_thick)./(d.tr_ma_11+d.tr_ma_12/d.rho/d.cspeed
+d.rho*d.cspeed*d.tr_ma_21+d.tr_ma_22); % transmission coefficient
d.trans_loss=20*log10(abs(1./d.trans_coef)); % [dB] transmission loss

% reflection coefficient, absorption coefficient, specific acoustic impedance
d.reflect_coef=(d.tr_ma_11+d.tr_ma_12/d.rho/d.cspeed-
d.rho*d.cspeed*d.tr_ma_21-
d.tr_ma_22)./(d.tr_ma_11+d.tr_ma_12/d.rho/d.cspeed+d.rho*d.cspeed*d.tr_ma_21+
d.tr_ma_22); % reflection coefficient
d.absorp_coef=1-abs(d.reflect_coef).^2; % aborption coefficient
d.spec_imp=(1+d.reflect_coef)./(1-d.reflect_coef); % specific acoustic
impedance

%% save data
if saveon==1
    d.data_filt=[];
    d.inst_mean=[];
    % drop original data and time series to reduce filesize
    d.data=[];
    d.time_series=[];
    save(d.filename,'d');
end

%% octave and one-third octave bands
ob=1e3*2.^[-6:4]; % octave band center frequencies [Hz]
ob_lo=ob./2.^(1/2); % octave band center frequency lower [Hz]
ob_hi=ob.*2.^(1/2); % octave band center frequency higher [hz]
otob=1e3*2.^([-18:12]/3); % one-third octave band center frequencies [Hz]
otob_lo=otob./2.^(1/6); % one-third octave center frequency lower [Hz]
otob_hi=otob.*2.^(1/6); % one-third octave center frequency higer [Hz]

% determine octave and one-third octave band transmission loss
% octave band
for jjj=1:length(ob)
ind1=max(find(d.f_ft<=ob_lo(jjj)));
ind2=max(find(d.f_ft<=ob_hi(jjj)));
ac_ob(jjj)=1/(ind2-ind1+1)*sum(d.trans_loss(ind1:ind2));
end
% one-third octave band
for jjj=1:length(otob)
ind1=max(find(d.f_ft<=otob_lo(jjj)));
ind2=max(find(d.f_ft<=otob_hi(jjj)));
ac_otob(jjj)= sum(abs(d.trans_loss(ind1:ind2)).^2);
end
```

6.3 Sample force transmissibility MATLAB code

```
%% data acquisition toolbox NI
clear all
warning off

%%
% preset post-processing built for constant-frequency & frequency-sweep
% experiments, for random experiments, and for ring-down experiments.

% the excitation parameters are not defined here, because they are presumed
% to either be nill (for 'ring-down') or governed by the vibration controller
% such as the Vibration Research VR9500

% thus, if using the controller for excitation purposes, the input
% parameters for the controller are determined via the post-processing
% here and the first channel is presumed to be the control accelerometer.

% for 'ring-down' type experiments, one must correctly identify the
% associated input channels with the responses of interest

%% acquire data?
dataacquire=1; % yes for acquire

%% post-processing relevant parameters
% test types are:
% 'sine' which is either frequency sweep or constant-frequency sinusoid
% 'random' which is random excitation
% 'ring-down' which are impulses on test components, used to determine
natural frequencies and damping ratios
% NOTE: each test may require a modified hi and lo frequency cutoff set for
the digital filtering
d.test_type='random';

%% test specimen name
d.specimen='10547_2x1x1_ft'; % specimen name, or no_specimen if none

%% data acquisition setup parameters
d.fs=8192; % sampling frequency [Hz]
d.wind=@hann; % window type for averages
d.seconds=60; % [s] seconds of data acquisition, determined according to
Vibration Research VR9500 controller test setup
d.filter_data_lo=10; % [Hz] of low pass cut off frequency
d.filter_data_hi=600; % [Hz] of high pass cut off frequency

%% fft computation parameters
% for 'sine' and 'random' tests only
% TIME_SAMPLED_PER_FFT is very important towards quality of post-processed
% data. If first attempt is not so great, try greater and lesser values.
d.time_sampled_per_fft=2; % [s] seconds of data acquisition over which fft is
evaluated
d.spacing_cts=round(d.fs*d.time_sampled_per_fft); % number of samples to use
in FFT to obtain freq_spacing
d.fft_numbers=floor(d.fs*d.seconds/d.spacing_cts); % number of ffts to
compute/loop through
```

```
d.nft=2^nextpow2(d.spacing_cts); % number of samples next to power of 2 for
spacing_cts

%% filename for save d structure
c=clock; % grab the time-stamp, eliminates possibility of data overwrite
d.filename=[num2str(c(1)) '_' num2str(c(2),'%02.0f') '_'
num2str(c(3),'%02.0f') '_' num2str(c(4),'%02.0f') num2str(c(5),'%02.0f') '_'
d.test_type '_' d.specimen '.mat'];
saveon=1; % save the data?

%% sensor sensitivity
d.sensor{1}='PCB_352C33_SN_LW194781_accelerometer_on_shaker_with_VR9500_contr
oller';
d.sensor{2}='PCB_208C02_SN_LW43427_force_transducer_input_from_shaker';
d.sensor{3}='PCB_208C01_SN_LW43812_force_transducer_output_at_base';
d.ch_sens(1)=1/.0533; % (m/s^2)/V  % PCB 333B40 accelerometer
d.ch_sens(2)=1/.01161; % N/V % PCB 208C02 force transducer
d.ch_sens(3)=1/.1125; % N/V % PCB 208C01 force transducer

%% mean sensor values [V] for each channel, to be subtracted from the input
before sensitivity to [units]
d.data_mean(1)=0; %
d.data_mean(2)=0; %
d.data_mean(3)=0; %

%% if for data acquisition
if dataacquire==1 % 1=yes for acquire

%% identify connected devices
devices=daq.getDevices;
% once obtained, ensure using correct device name in below session and
acquire lines

%% acquire data
s=daq.createSession('ni');
s.addAnalogInputChannel('Dev3',0,'Voltage'); % add input channels
s.addAnalogInputChannel('Dev3',6,'Voltage');
s.addAnalogInputChannel('Dev3',5,'Voltage');
s.Rate=d.fs; % set output and measuring frequency [Hz]
s.DurationInSeconds=d.seconds; % [s] duration of data acquisition
[d.data,d.time_series]=s.startForeground;
d.nn_chan=min(size(d.data));

%% bandpass filter data
clear ch_f
d.nn_chan=min(size(d.data));
myfilt=designfilt('bandpassiir','filterorder',4,'HalfPowerFrequency1',d.filte
r_data_lo,'HalfPowerFrequency2',d.filter_data_hi,'samplerate',d.fs);
for iii=1:d.nn_chan
ch_f(:,iii)=filtfilt(myfilt,d.ch_sens(iii)*(d.data(:,iii)-d.data_mean(iii)));
%
end

end
```

```
%%
d.data_filt=ch_f; % re-assign filtered data from local to structure variable

%% post-process data
%%
if strcmp(d.test_type,'sine')==1
%%
clear ch_ft gxy gxx coh tf y
d.inst_mean=[];d.f_ft=[];d.meansq=[];d.corr=[];d.lags=[];d.ch_ft_instavg=[];d
.freq_instavg=[];d.tf_est_instavg=[];d.gxx_instavg=[];d.gxy_instavg=[];
for ooo=1:2*d.fft_numbers-1 %  1:d.fft_numbers for no overlap.
1:2*d.fft_numbers-1 with half-overlap as defined below in trunc
    trunc=(ooo-1)*d.spacing_cts/2+1:ooo*d.spacing_cts/2+d.spacing_cts/2; %
define truncation in time : gives half-overlap of windowed averages is the
ooo=1:2*d.fft_numbers-1
    for iii=1:d.nn_chan
    d.inst_mean(ooo,iii)=mean(d.data_filt(trunc,iii)); % mean of
instantaneous data stream for the channel

y(:,iii)=fft(d.data_filt(trunc,iii).*window(d.wind,length(trunc)),d.nft)/(d.s
pacing_cts*mean(window(d.wind,length(trunc))));
%     y(:,iii)=fft(d.data_filt(trunc,iii),d.nft)/(d.spacing_cts); % take fast
fourier transform of data
    ch_ft(:,iii,ooo)=2*abs(y(1:d.nft/2+1,iii)); % magnitude of single-sided
fourier transform
    d.f_ft=d.fs/2*linspace(0,1,d.nft/2+1)'; % define frequency vector
    gxx(:,iii,ooo)=y(:,iii).*conj(y(:,iii))/2; % auto power spectrum
    if iii>0
    gxy(:,iii,ooo)=y(:,iii).*conj(y(:,1))/2; % cross power spectrum,
referencing input force
    end
    if iii>2

tf_est(:,iii,ooo)=tfestimate(d.data_filt(trunc,2),d.data_filt(trunc,iii),[],[
],d.nft,d.fs); % transfer function estimate
    end


    d.meansq(iii,ooo)=mean((d.data_filt(trunc,iii)-d.inst_mean(ooo,iii)).^2);
% mean-square system response [units]^2, with mean eliminated
    [d.corr(:,iii,ooo),d.lags]=xcorr(d.data_filt(trunc,iii)-
d.inst_mean(ooo,iii),d.data_filt(trunc,iii)-d.inst_mean(ooo,iii),'unbiased');
% autocorrelation of the signal
    end


    [mmx,ind]=max(squeeze(ch_ft(5:end,1,ooo))); % grab max and location of
max for first channel, control accelerometer, to identify the instantaneous
frequency [Hz]
    % the above look forward by 4 indices is to eliminate potential for high
DC component (due to signal shift) which will mislead results
    ind=ind+4; % look forward to accommodate above processing
    d.freq_instavg(ooo)=d.f_ft(ind); % [Hz] mean instantaneous excitation
frequency
    d.ch_ft_instavg(ooo,:)=max(squeeze(ch_ft(ind-2:ind+2,:,ooo)),[],1); % the
signals' FFT amplitude at this instantaneous frequency [units]
    d.gxx_instavg(ooo,:)=max(squeeze(gxx(ind-2:ind+2,:,ooo)),[],1); % the
signals' autospectral density at this instantaneous frequency [units^2]
```

```
    d.gxy_instavg(ooo,:)=max(squeeze(gxy(ind-2:ind+2,:,ooo)),[],1); % the
signals' cross spectral density at this instantaneous frequency [units^2]
    d.tf_est_instavg(ooo,:)=max(squeeze(tf_est(ind-2:ind+2,:,ooo)),[],1); %
the signals' transfer function at this instantaneous frequency [units^2]

    indt=ind; % hold index

end

%%
end
%%
%%
if strcmp(d.test_type,'random')==1
%%
clear ch_ft gxy gxx coh tf y
d.inst_mean=[];d.f_ft=[];d.ch_ft_a=[];d.gxx_a=[];d.gxy_a=[];d.tf_est_a=[];
for ooo=1:2*d.fft_numbers-1 %  1:d.fft_numbers for no overlap.
1:2*d.fft_numbers-1 with half-overlap as defined below in trunc
    trunc=(ooo-1)*d.spacing_cts/2+1:ooo*d.spacing_cts/2+d.spacing_cts/2; %
define truncation in time : gives half-overlap of windowed averages is the
ooo=1:2*d.fft_numbers-1
    for iii=1:d.nn_chan
    d.inst_mean(ooo,iii)=mean(d.data_filt(trunc,iii)); % mean of
instantaneous data stream for the channel

y(:,iii)=fft(d.data_filt(trunc,iii).*window(d.wind,length(trunc)),d.nft)/(d.s
pacing_cts*mean(window(d.wind,length(trunc))));
    ch_ft(:,iii,ooo)=2*abs(y(1:d.nft/2+1,iii)); % magnitude of single-sided
fourier transform
    d.f_ft=d.fs/2*linspace(0,1,d.nft/2+1)'; % define frequency vector
    gxx(:,iii,ooo)=y(:,iii).*conj(y(:,iii))/2; % auto power spectrum
    if iii>1
    gxy(:,iii,ooo)=y(:,2).*conj(y(:,iii))/2; % cross power spectrum,
referencing input force
    end
    if iii>2

tf_est(:,iii,ooo)=tfestimate(d.data_filt(trunc,2),d.data_filt(trunc,iii),[],[
],d.nft,d.fs); % transfer function estimate
    end
    end

end

for iii=1:d.nn_chan
d.ch_ft_a(:,iii)=mean(squeeze(ch_ft(1:d.nft/2+1,iii,:)),2); % average fft of
signal
d.gxx_a(:,iii)=mean(squeeze(gxx(1:d.nft/2+1,iii,:)),2); % average
autospectrum of signal
d.gxy_a(:,iii)=mean(squeeze(gxy(1:d.nft/2+1,iii,:)),2); % average
crosspectrum of signal
d.tf_est_a(:,iii)=mean(squeeze(tf_est(1:d.nft/2+1,iii,:)),2); % average
transfer functions
end
```

```
ob=1e3*2.^[-6:4]; % octave band center frequencies [Hz]
ob_lo=ob./2.^(1/2); % octave band center frequency lower [Hz]
ob_hi=ob.*2.^(1/2); % octave band center frequency higher [hz]
otob=1e3*2.^([-18:12]/3); % one-third octave band center frequencies [Hz]
otob_lo=otob./2.^(1/6); % one-third octave center frequency lower [Hz]
otob_hi=otob.*2.^(1/6); % one-third octave center frequency higer [Hz]

% determine octave and one-third octave band force transmissibility

% octave band
for jjj=1:length(ob)
ind1=max(find(d.f_ft<=ob_lo(jjj)));
ind2=max(find(d.f_ft<=ob_hi(jjj)));
tf_ob(jjj)=1/(ind2-ind1+1)*sum(abs(d.tf_est_a(ind1:ind2,3)).^2);
end
% one-third octave band
for jjj=1:length(otob)
ind1=max(find(d.f_ft<=otob_lo(jjj)));
ind2=max(find(d.f_ft<=otob_hi(jjj)));
tf_otob(jjj)= sum(abs(d.tf_est_a(ind1:ind2,3)).^2);
end

%%
end

%%
if strcmp(d.test_type,'ring-down')==1
%%
clear ch_ft gxy gxx coh tf y
% identify start and stop times
ind1=max(find(d.time_series<=14.6));
ind2=max(find(d.time_series<=15));
trunc=ind1:ind2;
d.nft=2^nextpow2(length(trunc)); % number of samples next to power of 2 for
spacing_cts
for iii=1:d.nn_chan

y(:,iii)=fft(d.data_filt(trunc,iii).*window(d.wind,length(trunc)),d.nft)/(len
gth(trunc)*mean(window(d.wind,length(trunc))));
    ch_ft(:,iii)=2*abs(y(1:d.nft/2+1,iii)); % magnitude of single-sided
fourier transform
    d.f_ft=d.fs/2*linspace(0,1,d.nft/2+1)'; % define frequency vector
end
d.f_ft=d.fs/2*linspace(0,1,d.nft/2+1)'; % define frequency vector

end

%% save data
if saveon==1
    d.data_filt=[];
    d.inst_mean=[];
    d.meansq=[];
    d.corr=[];
    d.lags=[];
    save(d.filename,'d');
end
```